OSLO METROPOLITAN UNIVERSITY
STORBYUNIVERSITETET

OsloMet – Oslo Metropolitan Univesity

Department of Civil Engineering and Energy Technologly
Mailing address: PB 4 St. Olavs plass, N-0130 Oslo, Norway
Street addresse: Pilestredet 35, Oslo

Phone 67 23 50 00
www.oslomet.no

GROUP NR.
1

AVAILABILITY
Open

MASTER THESIS

MASTER THESIS TITLE	DATE
POD-interpolation based analysis of indoor airflows	June 12, 2020
	NUMBEROF PAGES/ATTACHMENTS: 58/0
AUTHOR: Mats Kluftødegård	SUPERVISOR: Arnab Chaudhuri

DONE IN COLLABORATION WITH	CONTACT

ABSTRACT: This work reports a proper orthogonal decomposition (POD)-interpolation based prediction of indoor airflows related to displacement ventilation. Steady-state computational fluid dynamics (CFD) solution snapshots with varying relevant non-dimensional number are used to estimate the dominant POD coefficients/modal amplitudes and POD modes. A cubic spline interpolation of the POD coefficients is used to compute the solution for desired value of the non-dimensional number of interest. The verification and validation of this data-driven procedure is performed considering a 2D mixed convection problem involving a horizontal channel with cavity heated from below for a range of Richardson numbers. CFD solutions for a standard displacement ventilation configuration is then used to decompose the flow field variables in terms of Archimedes number dependent POD coefficients and associated space dependent POD bases. A detailed analysis of the CFD and POD-interpolated predicted flow-field variables for displacement ventilation cases, error estimates and the spatial structures of the POD modes are presented.

3 KEYWORDS
POD-interpolation
CFD
Indoor airflows

Preface

This master thesis represents the end of the degree "Energi og miljø i bygg – sivilingeniør" at Oslo Metropolitan university - storbyuniversitet. The work for this thesis have been done in the spring 2020.

First of all, I have to thank my great supervisor Arnab Chaudhuri. Since I met you autumn 2018, you have guided me, answered all my stupid questions, and given me opportunities to grow in the field of fluid mechanics. This thesis or the conference paper we delivered would not have been possible without you. Due to this weird spring we all have faced because of Covid-19, you have taken your time to have regularly meetings, regardless if it has been weekend, late evenings, what so ever. I think you should ask for a raise. So thanks for all the help Arnab.

Another person that has to be thanked is Dr. Marius Lysebo. I would like to say you took me under your wing during spring 2015, when I got the opportunity to be your assistant in the course EMTS1400 Thermodynamics. We have worked together through many courses and have made me evolve as an engineer and person. I would not be the engineer I am today without all guidance and discussion we have had about everything. I know you "like" things written a little bit cheesy Marius, but hope you know how much I appreciate all the help through all these years.

Last, but not least, thanks to Eivind Enget, my batchmate. The last two years have been easy, hard, exhausting, many words to describe it, but with you by my side for five years, it has been easier. Thanks for all the good projects we have delivered, and all the discussions about everything else.

So this is it, the end of all my years at OsloMet – Oslo Metropolitan Univesity, or as it have been called pretty much all the years I have been going there, "Høgskolen i Oslo og Akershus", thanks for five good years.

Contents

1 Introduction

Fundamentally, air flow, heat and mass transfer phenomena govern the indoor air quality, thermal comfort and energy usage in buildings. Air change rate, pollutant removal, heat removal, exposure and air distribution are the key features to assess the performance of a heating, ventilating and air-conditioning (HVAC) system. Ventilation systems can be classified into various types depending upon the concentration distribution, location of the air supply/exhaust device and the use of natural and mechanical forces ([4]). For several decades, a substantial scientific research focus has prevailed achieving design of energy efficient, effective airflow distribution and thermal comfort in buildings.

Displacement ventilation (DV) is potentially a very good ventilation strategy among the other types of air distribution such as natural ventilation or mixed ventilation. Natural ventilation is a principle which mainly don't use mechanical equipment, and mixing occurs when air is supplied high in the room, see section 1.1. DV-system, which is the main focus, the principles is where the contaminant air is removed from the ceiling level of a room. The exhaust temperature is higher than the occupied zone and a fresh air being supplied at the floor level ([20], [9], [21]). A well designed DV system can be energy efficient to regulate room temperature and air velocity for thermal comfort and good air quality utilising natural convection currents ([7]). Several key parameters for such systems are ventilation rate, location of the air terminal device, type of the diffuser and the supply air temperature ([31], [22]). Nevertheless, a DV configuration involves complex flow physics like gravity current, radiation effect and thermal stratification. Challenging issues related to thermal characterisation including radiation effects, draft discomfort, etc. are investigated by several researchers ([14], [5], [15], [11]). The recent studies with DV systems addresses interesting aspects considering e.g., severe odor problems in hospital environments ([8]), adaptive climate building with heat source/smart windows ([12]) and highly polluted indoor environment with dense oil mist in a machining plant ([30]). Optimal design and modeling aspects of DV systems in diverse contexts are therefore important active research areas for HVAC scientists and engineers.

Apart from the advanced experimental measurements, see figure 1, which can be time consuming and costly, CFD is widely used as a reliable numerical tool to predict a wide range of ventilation problems with detailed spatio-temporal distributions of flow-field variables. In CFD, the governing non-linear coupled partial differential equations are solved with a suitable discretization and solution procedure. However, high-fidelity CFD-simulations for design and optimization is indeed costly both in terms of necessary computer resource and CPU time. In this regard, proper orthogonal decomposition (POD) based interpolation can be used, exploiting the CFD results with varying one or many parameters (e.g. relevant non-dimensional numbers involved in the governing phenomena) of interest to produce desired predictions in an efficient and cost effective manner. For example, considering a set of steady-state CFD solutions as "snapshots" the dominant POD coefficients/modal amplitudes and POD modes have to be estimated first. These intern can be used with a suitable interpolation of the coefficients to generate desired solution(s) for particular values of the parameter(s) of interest without performing costly CFD simulations. Some of the previous studies used steady state CFD solutions as snapshots for POD e.g., in indoor airflow application (Elhadidi and Khalifa [10] and for coupling between CFD and lumped parameter flow network zonal (FNZ) models [13]).

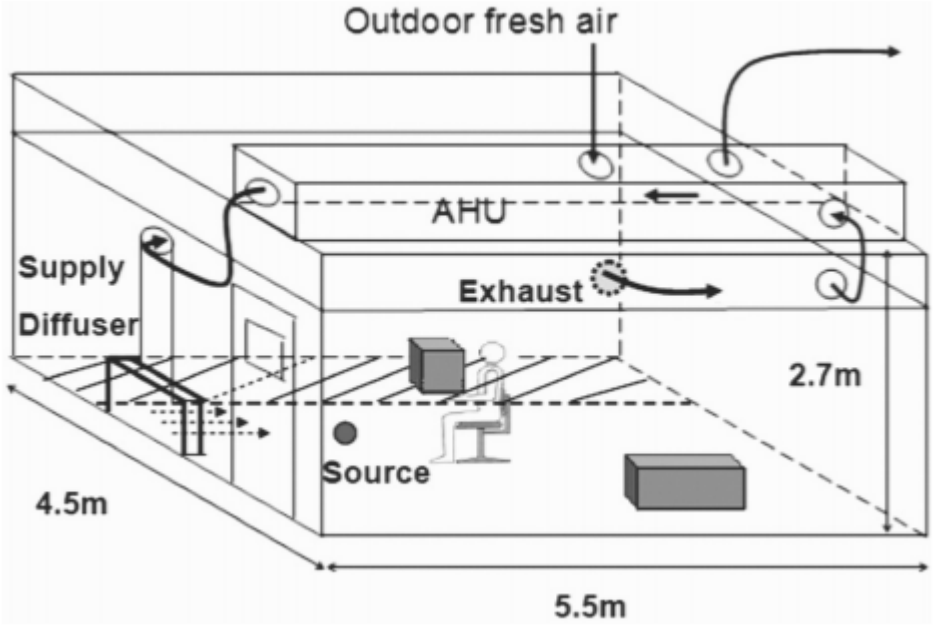

Figure 1: Experimental setup for DV-system example.[24]

This work aims to predict complex flow physics for a DV configuration of indoor environments using CFD snapshots and POD-interpolation method, and the objectives are presented in section 1.3. CFD results are generated using the commercial computer program StarCCM+. We solved 2D/3D compressible Navier-Stokes equation (without Boussinesq approximation) together with mass and energy equations. Additionally, two-equation turbulence models are employed to account turbulent flow cases. The thesis is organized as follows. First some background theory for DV-systems is introduced. In section Method, we present the governing equations, non-dimensional numbers and the overall POD methodology. The validation cases are presented thereafter. Subsequently, the problem setup of the displacement ventilation is given. The flow analysis given in the section Results and discussion. Finally, the conclusions are drawn at the end.

1.1 Displacement ventilation

There are to main mechanical design of ventilation systems, displacement and mixing. In mixing ventilation (MV) air is supplied high in the room, and induce the room air and the air gets mixed, see figure 2. On the other hand, in displacement ventilation (DV) air is supplied low on the floor level, with low velocity and lower temperature than the room, see figure 3. ([20], [9], [21]) This thesis is going to focus on the DV-system.

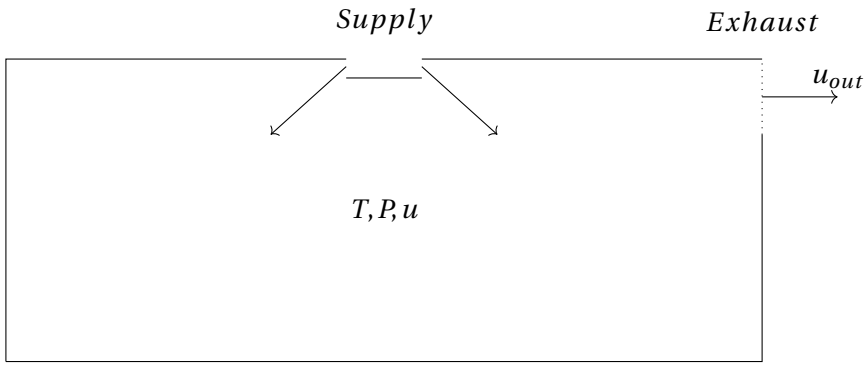

Figure 2: Illustration of a MV-system: P is pressure, T is temperature and u is velocity.

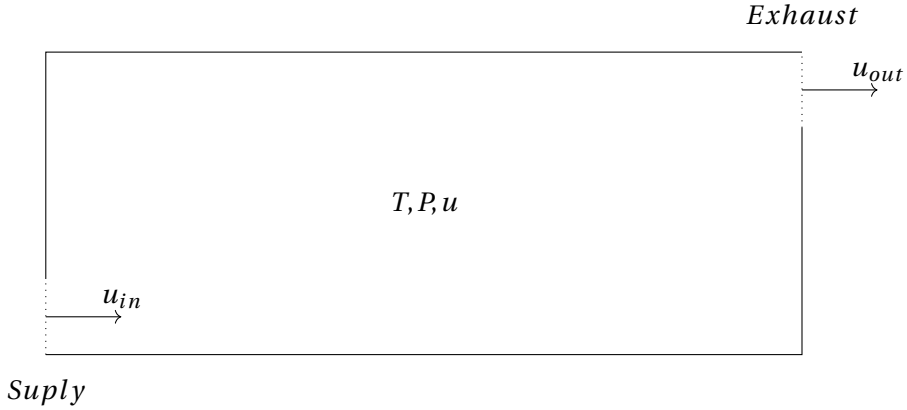

Figure 3: Illustration of a DV-system: P is pressure, T is temperature and u is velocity.

The physics behind DV-systems is that the buoyancy forces are used to get air moving upwards from the ground since hot air has lower density than cold air which is supplied at the floor level. The air distribution to the room happens through the air diffuser at the floor as mentioned earlier. The main physics in the diffuser region is divided into three zones, see figure 4.

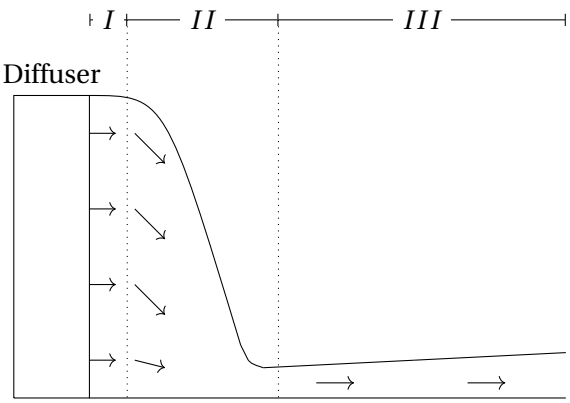

Figure 4: Illustration of physics near a DV-system inlet diffuser. [23]

The three phases are:

I) Establishment zone. Here, the entry velocity is defined and how it induces the room air is dependent on the design of the diffuser.

II) Acceleration zone. The air accelerates due to temperature difference between the diffuser air at the inlet and the room air.

III) Gravitational zone. After a while, the air velocity will slow down and be heated by the room air. When air hits the wall at some point, the air will move backwards and we will get the typical stratification for DV-systems.

A interesting point about DV-systems is that the maximum air velocity in the DV diffuser region is not at the inlet, but in the transition between phase II and III, due to temperature differences between room air and inlet air. [23] Illustrations at the inlet region for a experimental setup for a DV-system to demonstrate the establishment zone can be seen in figure 5 and 6.

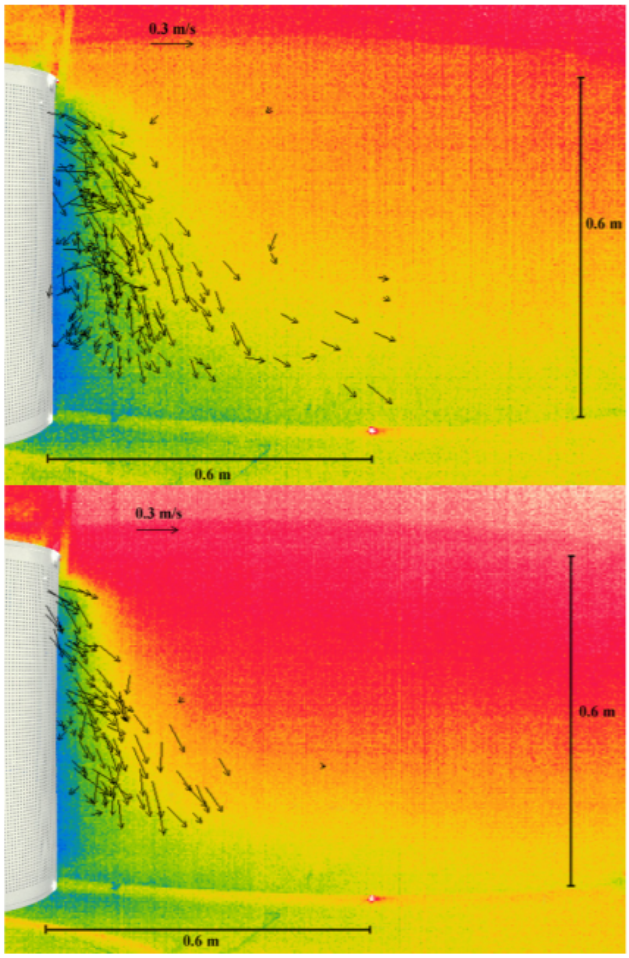

Figure 5: Temperature distribution and velocity vectors for experimental setup for different Archimedes numbers ($Ar = 0.32$ (top) and $Ar = 0.47$ (bottom)). [Picture source: Cehlin [6]]

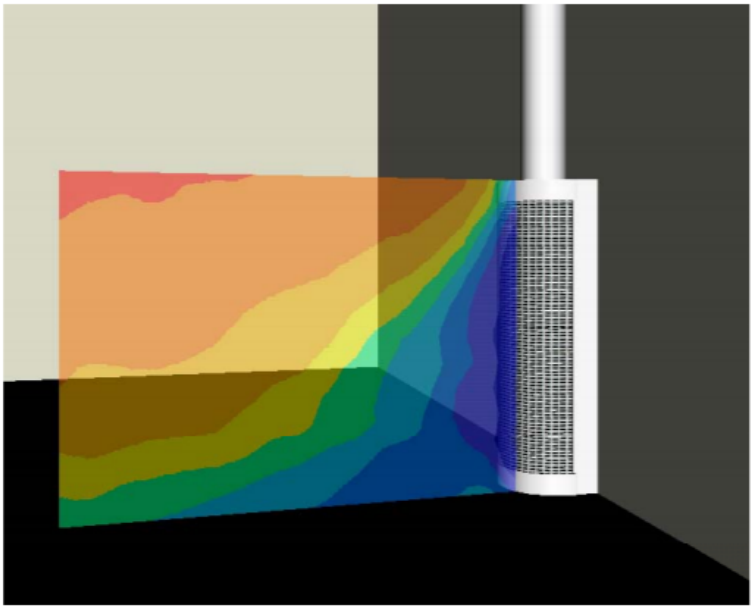

Figure 6: Temperature distribution at the diffuser inlet.[Picture source: Cehlin [6]]

The design of the diffuser for DV-systems have a impact on the distibution of the air. Therefore there is plenty of different designs, see figure 7. The main idea for the diffuser design is that some ventilation channel with fresh air is supplied in it, and the front of the diffuser is perforated with holes for distribution of air in the room. If the diffuser have linear or radial distribution depends on the room.

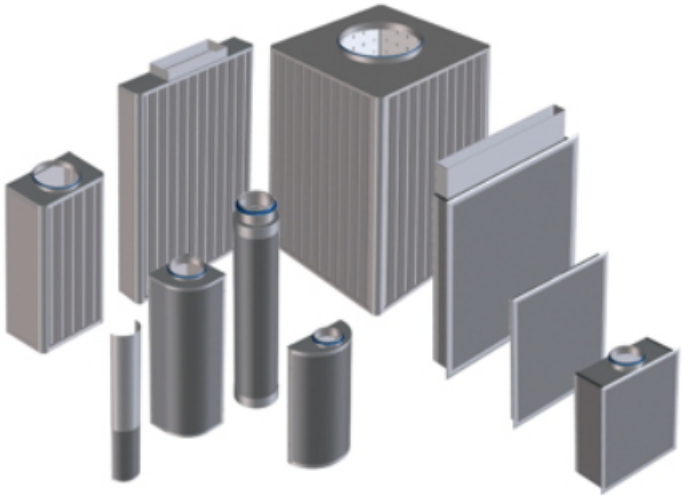

Figure 7: Diffuser design for DV-system.[19]

The beneficial point about DV-systems as mentioned in the introduction is that it has the possibility of almost removing all the contamination in the room. However, to achieve this, strict criteria for engineering has to been followed, and many things can destroy this ventilation principle. Such as obstacels in front of the diffuser, to high inlet velocity which would ruin the thermal comfort in the near zone of the diffuser.

Further in the thesis, results from CFD simulations of a DV-system will be presented, where this main principles of the system will be shown, such as good stratification and acceleration zone.

1.2 CFD vs experimental setup

In this thesis the data for the POD analysis will be generated by CFD simulations for a DV-system. The other option could be to perform experiments, which is also possible while using POD based interpolation method for the data extracted from experimental results. CFD have the possibility to perform simulations for large scaled models, while experimental setup have scales limited by the laboratories. Also CFD has the advantages of saving time, and is not costly in form of necessary equipment. An image by Arghand et al. [2], is representative depicting how complex an experimental setup can be, see figure 8.

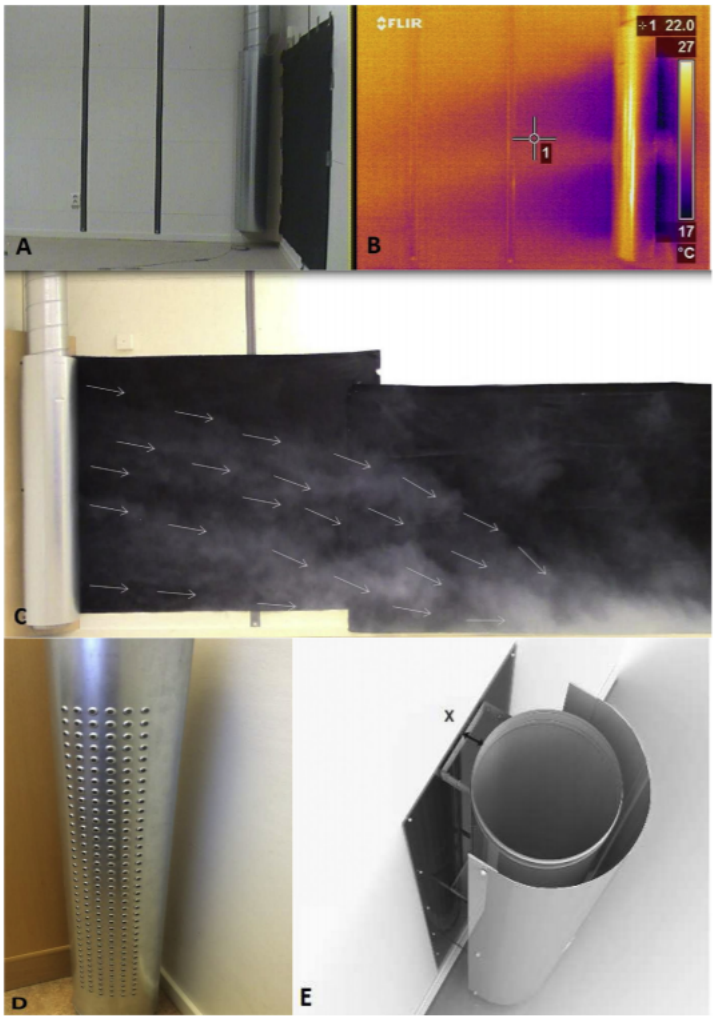

Figure 8: Experimental setup for a DV-system showing diffuser, flow distribution at the inlet with smoke vizualization.[Picture source: Arghand et al. [2]]

1.3 Objective

The focus for the thesis is to apply POD-interpolation method in predicting complex flow physics for a displacement ventilation system, and therefore CPU time and requirement of computer resources could be reduced significantly. The objectives of the thesis are:

- Overall implementation of data driven POD-interpolation method in python.
- Validation of the POD-interpolation method, with CFD solution snapshots for a benchmark test case involving relevant flow physics.
- Analysis of displacement ventilation system after obtaining snapshots from CFD simulations for different Archimedes numbers.
- POD analysis, comparing CFD snapshots with results obtained by the POD-interpolation method.

2 Method

In this section the method for the thesis is presented. This involves presentation of the governing equations of the fluid flow, introduction of the tool used for simulations, and the description of the method, POD-interpolation method.

2.1 Governing equations

The physical model that is defined is based on solving governing equations that describes fluid flow. This involves solving compressible Navier-Stokes equations together with the mass and the energy conservation equations. Continuity equation is given by:

$$\frac{\partial \rho}{\partial t} + \nabla \cdot (\rho \mathbf{u}) = 0 \tag{1}$$

Where ρ is the density, $\mathbf{u}$ the velocity vector and t the time. This equation is three-dimensional and unsteady for a compressible fluid.

Momentum equation is defined as the momentum of the flow depending on the forces acting on the fluid. Defined as:

$$\frac{D(\rho \mathbf{u})}{Dt} = -\frac{\partial p}{\partial \mathbf{x}} + \nabla \cdot (\mu \nabla \mathbf{u}) + S_M \tag{2}$$

Where p is the pressure, μ is the dynamic viscosity and S_M is the source term, for example gravity. This is important for DV-systems, since gravity is an acting force on the fluid in DV-systems.
Applying the first law of thermodynamics on a control volume, we can write the conservation of energy as:

$$\frac{D(\rho E)}{Dt} = -p\nabla \cdot \mathbf{u} + \nabla \cdot (k \nabla T) + S_e + \Phi \tag{3}$$

Where E is energy, k the thermal conductivity of the fluid, T the temperature, S_e is energy source term and Φ is dissipation term due to deformation work.
The working fluid is air which can be treated as ideal gas, with equation of state.

$$p = \rho R T \tag{4}$$

Where p is pressure, R is ideals gas constant, ρ is density and T is temperature.

The governing equations above, equation (1), (2) and (3), can be written in a general form called the transport equation for any conserved property as:

$$\frac{D(\rho \phi \mathbf{u})}{Dt} = \nabla \cdot (\Gamma \nabla \phi) + S_\phi \tag{5}$$

Where ϕ is some scalar property, Γ is diffusion coefficient. The governing equation involves advection term in left hand side and the terms on the right hand side signify the diffusion term and the generation term respectively.

To write the governing equations in a more compact form, the material derivative or advective

derivative, it has many names, is used. It describes the time rate of change for some proprerty, ϕ, and can be extended to:

$$\frac{D(\rho\phi\mathbf{u})}{Dt} = \frac{\partial(\rho\phi)}{\partial t} + \nabla\cdot(\rho\phi\mathbf{u}) \tag{6}$$

This junction involves the transient term of the governing equation and the convective term. Its a mote compact way to write governing equations.
In general CFD techniques can solve this equations. For turbulent flows, Reynolds averaged Navier-Stokes can be used. [28]

2.2 Reynolds-Averaged Navier-Stokes (RANS)

Usually, CFD omit solves time-averaged properties for the flow, witch means they solve mean velocity, mean stresses and mean pressures. Therefore, turbulent flow is mostly simulated with Reynolds-Averaged Navier-Stokes equations or RANS. This takes the governing equations as described in previous section, where flow properties is replaced with the sum of the mean and a fluctuating component such as:

$$\mathbf{u} = \mathbf{U} + \mathbf{u}' \tag{7}$$
$$u = U + u' \tag{8}$$
$$v = V + v' \tag{9}$$
$$w = W + w' \tag{10}$$
$$p = P + p' \tag{11}$$
$$\tag{12}$$

Then the continuity equation becomes:

$$\frac{\partial\overline{\rho}}{\partial t} + \nabla\cdot(\overline{\rho}\widetilde{\mathbf{u}}) = 0 \tag{13}$$

RANS equations as:

$$\frac{\partial(\overline{\rho}\widetilde{U})}{\partial t} + \nabla\cdot(\overline{\rho}\widetilde{U}\widetilde{\mathbf{u}}) = -\frac{\partial\overline{p}}{\partial x} + \nabla\cdot(\mu\nabla\widetilde{U}) + \left[-\frac{\partial(\overline{\overline{\rho}u'^2})}{\partial x} - \frac{\partial(\overline{\overline{\rho}u'v'})}{\partial y} - \frac{\partial(\overline{\overline{\rho}u'w'})}{\partial z}\right] + S_{Mx} \tag{14}$$

$$\frac{\partial(\overline{\rho}\widetilde{U})}{\partial t} + \nabla\cdot(\overline{\rho}\widetilde{V}\widetilde{\mathbf{u}}) = -\frac{\partial\overline{p}}{\partial y} + \nabla\cdot(\mu\nabla\widetilde{V}) + \left[-\frac{\partial(\overline{\overline{\rho}u'v'})}{\partial x} - \frac{\partial(\overline{\overline{\rho}v'^2})}{\partial y} - \frac{\partial(\overline{\overline{\rho}v'w'})}{\partial z}\right] + S_{My} \tag{15}$$

$$\frac{\partial(\overline{\rho}\widetilde{W})}{\partial t} + \nabla\cdot(\overline{\rho}\widetilde{W}\widetilde{\mathbf{u}}) = -\frac{\partial\overline{p}}{\partial z} + \nabla\cdot(\mu\nabla\widetilde{W}) + \left[-\frac{\partial(\overline{\overline{\rho}u'w'})}{\partial x} - \frac{\partial(\overline{\overline{\rho}v'w'})}{\partial y} - \frac{\partial(\overline{\overline{\rho}w'^2})}{\partial z}\right] + S_{Mz} \tag{16}$$

Similar the transport equations is derived with adding fluctuating term and take the time-averaged of a scalar property, ϕ:

$$\frac{\partial(\overline{\rho}\widetilde{\Phi})}{\partial t} + \nabla\cdot(\overline{\rho}\widetilde{\Phi}\widetilde{\mathbf{u}}) = \nabla\cdot(\overline{\rho}\nabla\widetilde{\Phi}) + \left[-\frac{\partial(\overline{\overline{\rho}u'\phi'})}{\partial x} - \frac{\partial(\overline{\overline{\rho}v'\phi'})}{\partial y} - \frac{\partial(\overline{\overline{\rho}w'\phi'})}{\partial z}\right] + S_{\Phi} \tag{17}$$

In the equations above, the overbar indicates a time-averaged variable and the tilde indicates a density-weighted or Favre-averaged variable. [28] To calculate RANS equations, turbulence modelling is needed. This is since number of unknowns in the above equation exceeds the number of equations, and therefore its needed additional equations, which we get from turbulence modelling. This is presented in the next section.

2.3 Turbulence model

As mentioned in previous section, turbulence modelling is needed to solve RANS equation. There are many different turbulence models out there but depending on the problem a suitable model has to be chosen. For good prediction of air flows in a DV-system, we need to choose a model that can describe the air flows behavior well. To describe if the flow is either turbulent or laminar, the dimensionless number Reynolds number (Re) is used, see section 2.5.2. When having high Reynolds numbers the flow can be stated to be turbulent, where the flow is chaotic and the motions is random. Then we need a turbulence model in CFD software to describe this behavior.[28]

The two main turbulence models used in CFD-simualtions for DV-systems is the SST (Menter) $\kappa-\omega$ and $\kappa-\epsilon$ models.
SST (Menter) $\kappa-\omega$ is a two equation model, where the turbulent kinetic flow, κ and the specific dissipation, ω -equations are solved for the flow. Th governing equation for this model is formulated as:

$$\frac{\partial(\rho k)}{\partial t}+\nabla\cdot(\rho k\mathbf{U})=\nabla\cdot\left[\left(\mu+\frac{\mu_t}{\sigma_k}\right)\nabla k\right]+P_k-\beta^*\rho k\omega \tag{18}$$

$$\frac{\partial(\rho\omega)}{\partial t}+\nabla\cdot(\rho\omega\mathbf{U})=\nabla\cdot\left[\left(\mu+\frac{\mu_t}{\sigma_{\omega,1}}\right)\nabla\omega\right]+\gamma_2\left(2\rho S_{ij}\cdot S_{ij}-\frac{2}{3}\rho\omega\frac{\partial U_i}{\partial x_j}\delta_{ij}\right)-\beta_2\rho\omega^2+2\frac{\rho}{\sigma_{\omega,2}\omega}\frac{\partial k}{\partial x_k}\frac{\partial\omega}{\partial x_k} \tag{19}$$

Where σ_ω, $\sigma_{\omega,1}$, $\sigma_{\omega,2}$, β^*, β_2 and γ_2 is constants for the turbulence model given in Versteeg and Malalasekera [28, p.92], μ is dynamic viscosity, and μ_t is the eddy viscosity given by:

$$\mu_t=\frac{\rho k}{\omega} \tag{20}$$

The other model thats been widely used for DV-system simulations, is $\kappa-\epsilon$. This is also a two equation model, where the main difference between equations is the last term in equation (19). This comes from the adjustment between the two models, where SST (Menter) $\kappa-\omega$ substitutes the ϵ with $k\omega$ and gives an extra term, as mentioned above, the cross-diffusion term. Therefore, for describing difference between $\kappa-\epsilon$ and SST $\kappa-\omega$ in a CFD problem, the difference lies in the near wall treatment. This is since the $\kappa-\epsilon$ model shows unsatisfactory for the boundary layer with adverse pressure gradient, and $\kappa-\omega$ is adjusted to predict this better. [28]

There has been done several studies of DV-systems in interest of finding the best turbulence model, which give the most accurate results for these kinds of problem. Menchaca Brandan [17] used the $\kappa-\epsilon$ for his studies of a natural ventilation system, and gave good results for different Archimedes numbers and for thermal stratification in the room. Later on Gilani et al. [11] has done sensitivity analysis of DV-systems with use of different turbulence models, such as $\kappa-\epsilon$ which was used by Menchaca Brandan [17]. Their study shows that SST (Menter) $\kappa-\omega$ gives better results for DV-systems then $\kappa-\epsilon$ compared with experimental data and is therefore used in this thesis.

At the inlet boundary condition there has been pre-calculated values for turbulent kinetic flow and specific dissipation rate, see section 5.1.

2.4 Near wall treatment

Turbulence near wall plays an important role in CFD. Since the flow is interacting with solid surface instead of being free turbulent flow, the flow will behave differently, and models to describe this is

needed. If a Reynolds number is formed with a distance, y, from the wall we get the formulation:

$$Re_y = \frac{Uy}{\nu} \tag{21}$$

Where μ is kinematic viscosity, U is velocity and y is some distance from the wall. This initiates that closer to the wall the lower the Reynolds number would be, and the viscous effects are more dominant. [28] A suitable y^+ wall treatment was used in this thesis.

2.5 Non-dimensional numbers

This thesis is focusing on Non-dimensional numbers to be used in the later on described POD-method, which is used for describing the physical phenomena of a problem and has impact on the governing equations. This is interesting since it can help us understanding a phenomena, such as the behavior of a DV-system that is of interest in this thesis.

DV-systems affects the indoor airflows, and we therefore has to find non-dimensional numbers of interest to this kind of problem. Therefore, below there is presented some non-dimensional numbers of interest, where our main focus is the Archimedes numbers.

2.5.1 Grashof number

Grashof number is a dimensionless number which gives the ratio between the buoyancy and viscous forces acting on a fluid. It is defined as follow in eq. (22).

$$Gr = \frac{g\beta\Delta T L^3}{\nu^2} \tag{22}$$

Where g is the acceleration due to gravity, β is the thermal expansion coefficient, ΔT is the temperature difference between inlet and outlet, L is the characteristic height of the inlet and μ is the kinematic viscosity of the fluid.

2.5.2 Reynolds number

We divide flow into two category's, turbulent or laminar flow. Between these you have a transition region, see figure 9.

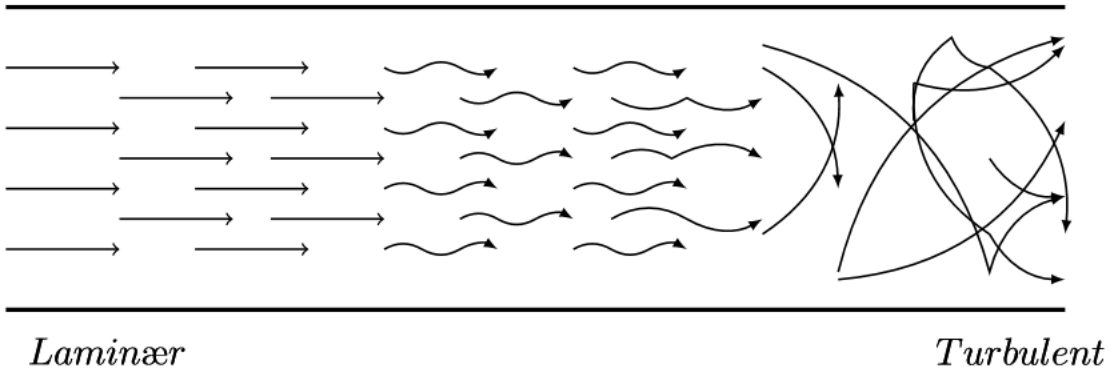

Figure 9: Image for laminar and turbulent flow.

To define if the flow is turbulent or laminar we define a dimensionless number called the Reynold number (Re), which is the ratio between inertia forces and viscous forces. The definition of this is:

$$Re_L = \frac{uL}{\nu} \tag{23}$$

Where u is the velocity of the fluid, L is the characteristic length and ν the kinematic viscosity. For large Reynolds number above 2900 you will have turbulent flow for pipe flow, and for low numbers below 2300 you will have laminar flow for pipe flow.

2.5.3 Archimedes number

Archimedes number is a ratio between buoyancy and momentum forces acting on a fluid. This can be used to determine the thermal stratification in a room, therefore important for a DV-system. Here in the next sub sections some different formulas for Archimedes is presented. It's mainly a ratio between Grashof number, and Reynolds number squared. This is given by:

$$Ar = \frac{Gr}{Re^2} = \frac{g\beta\Delta TL}{u^2} \tag{24}$$

Archimedes number can help predicting the thermal stratification in a room as mentioned, this has been shown in earlier litterature. [17, 20] This is a useful number for displacement ventilation, and rewriting the equation can give a more useful equation since the temperature difference in the room (ΔT) is dependent on the flow rate ($\dot{V} = A_s u$) through the room and the heat gain (q_t) in the room, where total heat gain is defined as:

$$q_t = \rho c_p \dot{V} \Delta T \tag{25}$$

$$\Delta T = \frac{q_t}{\rho c_p \dot{V}} \tag{26}$$

Where ρ is fluid density c_p is specific heat capacity, A_s is area of inlet diffuser and u is inlet velocity. This makes us available to rewrite eqn. (24):

$$Ar = \frac{g\beta\Delta TL}{u^2} \tag{27}$$

$$= \frac{g\beta}{\rho c_p} \frac{q_t L}{u^2 \dot{V}} \tag{28}$$

$$= \frac{g\beta}{\rho c_p} \frac{q_t L}{u^3 A_s} \tag{29}$$

This equation takes into account the heat gain in the room, instead of temperature difference in the room. This can be easier, when we dont know the outlet temperature which is the usual case. Equation (29) was presented by Menchaca Brandan [17] and is used in this thesis for calculation of the velocity at the inlet for chossen Archimedes number.

2.5.4 Nordtest method "Dimensionless" Archimedes number

In the CFD-simulation subsequent in this thesis, we are using the setup following the prescription of the Nordtest method. For the analysis of a DV-system, they have proposed a set of equation for dimensioning displacement ventilation for different type of diffusers, radial and linear. [22]

Nordtest method came up with an semi-empirical formula for max velocity along floor with two correlation coefficients, $k_{1,max}$ and $k_{2,max}$.

$$v_{max} \approx k_{1,max} \cdot Ar^{k_{2,max}} \cdot B \tag{30}$$

This is an equation for curvefitting, after obtaining data from CFD or experimental setups. The coefficient can then be found for a setup, when obtaining all data needed in the formula, and then describe the flow with the function.[22]
Archimedes number (Ar) proposed in the Nordtest method and B is the buoyancy flux, eq. 31 and 32.

$$Ar = \begin{cases} \frac{g' L^5}{\dot{V}^2} & \text{for radial ATDs} \\ \frac{g' L^2}{\dot{V}^2} & \text{for linear ATDs} \end{cases} \tag{31}$$

$$B = \left(\frac{\dot{V} g'}{L} \right)^{1/3} \tag{32}$$

Where g' is the reduced gravity $[m/s^2]$, L is horizontal parameter of outlet area $[m]$ and $\dot{V}$ is total air volume flow rate $[m^3/s]$. Where reduced gravity is given as:

$$g' = 9.81 \frac{\Delta\theta_t}{\theta_r} \tag{33}$$

Where $\Delta\theta_t$ is total air temperature difference in room (θ_i-θ_t) and θ_r is reference temperature in room in Kelvin.
The main idea here is that Nordtest method has proposed a set of equations, defined from experimental setup for a DV-system. Later on we will look into this formula, comparing the Archimedes number from this section and the one obtained in the previous section, equation (29) by Menchaca Brandan [17].

2.6 Computational fluid dynamics

Computational fluid dyamics or CFD, is the analysis of a system involving heat transfer, fluid flow and similar phenomena using computer based simulation. [28, p.1]. This is widely used in the industry with different areas of application such as aerodymanics for windmills, aircrafts etc, hydrodynamics for ships and inside many other areas. For our purpose we are interested in DV-system, which involves both fluid flow and heat transfer problems, and CFD is therefore a good tool for this purpose.

In this thesis we are using the program, Star CCM+. The main steps in a process of solving a problem with CFD are the three phases: Pre-processor, solver and Post-processor. [28]

First, in Pre-processor the computational domain is defined. This involves making the geometry of the problem setup with sufficient mesh. Mesh is the control volumes we divide a problem setup into, where governing equations are solved for properties of interest. A good prediction of a problem, demands a good quality mesh, where its representative to real physics. This involves having finer mesh in regions where there is larger variations in the properties from point to point.[28]

The next part is the solver. Most of the CFD tools uses the finite volume method (FVM) based solver. This involves integration of the governing equations inside a control volume, taking the resulting equations into a system of equations, and solves this usually with a iterative method. Different type of solvers can be used, depending on the problem, such as different turbulence models, models for near wall treatment etc.

The last process is the Post-processor. When results is obtained, the results has to be analysed and/or visualized. This can be in form of XY-plots, vector/scalar plots, streamlines etc. Many ways to analyse a problem, dependent on the intention of a study. In this thesis, there is of interest in using POD interpolation method in the post processor phase. More about this is presented later in the thesis.

In our solver, when running steady state simulations in Star-CCM+ we used second order implicit segregated or coupled flow solvers equipped with Roe schemes for convection, hybrid Gauss least-squared gradient method based 2nd order schemes for diffusion and Venkatakrisnan limiter function are chosen. Algebraic Multi-Grid (AMG) techniques are also invoked with the setup mentioned above.

3 Data analysis and machine learning

The world has seen a large increase in data in different scientific areas, for example in fluid mechanics. Interest in extracting information from the data, have made people interested in the field of machine learning, and there have been great progress in this field over the past years. From definition, machine learning is algorithms that process and extract information from a set of data. It can for example be from some data giving information about peoples shopping habits, which grocery is the most popular ones among people. [Brunton et al. [3]]

These algorithms used in machine learning are divided into three categories: Supervised-, semi-supervised and unsupervised-learning. Which one to use depends on the information available in the data. This thesis is going to use an algorithm which essentially falls in the unsupervised category. [3]

3.1 Unsupervised learning

Unsupervised learning is a method that finds unknown patterns that wasn't know from before. This is different from supervised learning, where supervised learning is given some data with correct knowledge and learns from that. Adding new data to a supervised model, the machine will recognise patters from the correct knowledge it has been fed, and therefore learn it self to recognise patterns. To the unsupervised algorithm you are feeding some data, the algorithm process and you get some extracted output, without the need for supervision. [3]

A well known method of unsupervised learning is PCA or Principal component analysis. This is a statistical operation, where it uses a orthogonal transformation to convert data of correlated variables into a set of linearly uncorrelated variables. Orthogonal transformation is in linear algebra an operation to preserve a vectors length and angles between them.
One method, closely related to PCA, is POD method. In this thesis POD snapshot method is used, and was presented by Sirovich [26]. A brief account of the method is presented in the next section.

3.2 POD snapshot method

Due to high computational costs running numerical simulations, proper orthogonal decomposition (POD) method has been used to produce reduced-order models (ROMs). The method takes a set of POD basis from given data from a numerical simulation or experiments, and uses this to construct state variable approximations. The method mainly extracts basis functions containing characteristics of the system of interest. [29]

3.2.1 Computing POD modes

Proper orthogonal decomposition (POD) method can be realized in several forms such as Karhunen-Loève decomposition (KLD), principal component analysis (PCA), and singular value decomposition (SVD) having wide spectrum of applications in scientific and engineering field. The key dominant characteristics/features in a data set can be recognized by a POD technique via low-dimensional descriptions for multidimensional systems. Originally, POD was introduced in the framework of fluid mechanics applications in late sixties. This was followed by the "snapshot POD" methodology by Sirovich and Kirby [27] and the procedure is essentially a simple data-driven procedure closely related to principal component analysis (PCA), one of the fundamental algorithm of

applied statistics and machine learning ([3]). In this work, the steady-state CFD solutions "snapshots" are used to decompose a non-dimensional flow variable $\phi^*(\Pi, \vec{x})$, where Π is a governing non-dimensional number of the flow physics under consideration. The decomposition essentially leads to the determination of a finite number of POD coefficients, $a_k(\Pi)$ and space dependent POD modes, $\psi_k(\vec{x})$ as,

$$\phi^*(\Pi, \vec{x}) \approx \sum_{k=1}^{m} a_k(\Pi)\psi_k(\vec{x}). \tag{34}$$

where, m is the number of snapshots for set of values of $\Pi_i \in [\Pi_{min}, \Pi_{max}]$, $\forall\ i = 1, \ldots, m$. Once, the desired POD coefficients and POD modes are available, a suitable interpolation can be used to construct the flow field variables for any intermediate Π_{int}. The POD-interpolated prediction can be given by

$$\phi^*(\Pi_{int}, \vec{x}) \approx \sum_{k=1}^{N} a_k(\Pi_{int})\psi_k(\vec{x}). \tag{35}$$

where $N \leq m$. More about the interpolation is given in section 3.2.2.

A brief methodology to determine the POD coefficients and the POD modes is given below (see Meyer et al. [18], Selimefendigil [25] for detail). First, the m number of CFD solution of ϕ^* on n mesh points can be arranged in a data set matrix $\mathbf{\Phi}^* = [\boldsymbol{\phi}^{*1}\boldsymbol{\phi}^{*2}\ldots\boldsymbol{\phi}^{*m}]$ as,

$$\mathbf{\Phi}^* = \begin{bmatrix} \phi_1^{*1} & \phi_1^{*2} & \phi_1^{*3} & \ldots & \phi_1^{*m} \\ \phi_2^{*1} & \phi_2^{*2} & \phi_2^{*3} & \ldots & \phi_2^{*m} \\ \vdots & \vdots & \vdots & \vdots & \vdots \\ \phi_n^{*1} & \phi_n^{*2} & \phi_n^{*3} & \ldots & \phi_n^{*m} \end{bmatrix}. \tag{36}$$

Then the auto covariance matrix is created. This matrix represents the covariance of the value with it self at some point. Where covariance is a measure of the linear dependency of two values. This can be defined as:

$$\mathbf{C} = \frac{1}{m}\mathbf{\Phi}^{*^\intercal}\mathbf{\Phi}^*. \tag{37}$$

The following eigenvalue problem then has to be solved:

$$\mathbf{C}\mathbf{X}^i = \lambda^i\mathbf{X}^i, \quad i = 1, 2, ..., m. \tag{38}$$

Where $\mathbf{X}$ is the eigenvector, and λ is the eigenvalues. This eigenvalue problem was solved using singular value decomposition (SVD). The solutions are ordered according to the size of the eigenvalues from highest to lowest, where higher values indicates higher containment of energy. The eigenvectors, $\mathbf{X}^i$, in equation (38) forms a basis for making the POD modes, $\boldsymbol{\psi}^i$:

$$\boldsymbol{\psi}^i = \frac{\sum_{j=1}^{m} X_j^i \boldsymbol{\phi}^{*j}}{\left\| \sum_{j=1}^{m} X_j^i \boldsymbol{\phi}^{*j} \right\|}, \quad i = 1, 2, ..., m. \tag{39}$$

Where X_j^i is the j'th component of the eigenvector corresponding to the eigenvalue λ^i, and $\|\cdot\|$ is the second norm of any vector $\boldsymbol{\xi}$, given as:

$$\|\boldsymbol{\xi}\| = \sqrt{(\xi_1)^2 + (\xi_2)^2 + ... + (\xi_n)^2} \tag{40}$$

The POD coefficient can be determined by projecting $\boldsymbol{\phi}^{*m}$ onto the POD modes:

$$\mathbf{a}^m = \Psi \boldsymbol{\phi}^{*m} \tag{41}$$

Where $\Psi = [\boldsymbol{\psi}^1 \boldsymbol{\psi}^2 \dots \boldsymbol{\psi}^m]$ The snapshot $\boldsymbol{\phi}^{*m}$ can then be reconstructed by:

$$\boldsymbol{\phi}^{*m} = \Psi^\intercal \mathbf{a}^m \tag{42}$$

Due to conservation of energy, the first modes will contain most of the energy. Therefore results can be reproduced with use of fewer modes, where energy conserved is above 99 %, will probably give good approximation. This is defined such as if the sum of number of eigenvalues, λ, divided by the sum of all eigenvalues is above 99%:

$$E_r = \frac{\lambda^i}{\sum_{i=1}^m \lambda^i} > 0.99 \tag{43}$$

This can reduce computational time, and still give good predictions of the problem.
The above methodology has been implemented via Python programming scripts.

3.2.2 Interpolation of POD coefficients

As described in section 3.2.1, we have to use interpolation methods to estimate $a_k(\Pi_{int})$ from $a_k(\Pi_i)$'s. In this thesis we used cubic spline interpolation to find the POD coefficients. The main idea behind the cubic spline interpolation method, is that it is a piece wise continuous curve, passing through each of the values of a dataset [16].

Let us assume that $\Pi_i < \Pi_{int} < \Pi_{i+1}$, for $i = 1,2,...m-1$. Then the cubic spline interpolation method to estimate $a_k(\Pi_{int})$ can be given by:

$$a_k(\Pi_{int}) = c1_k(\Pi_{int} - \Pi_i)^3 + c2_k(\Pi_{int} - \Pi_i)^2 + c3_k(\Pi_{int} - \Pi_i) + c4_k, \qquad k = 1,2,...,m \tag{44}$$

Where the m is number of points to interpolate between. The derivatives of $a_k(\Pi)$ are needed to estimate the values of the coefficients, $c1_k$, $c2_k$, $c3_k$ and $c4_k$, using discrete values of $a_k(\Pi_i)$ [16].

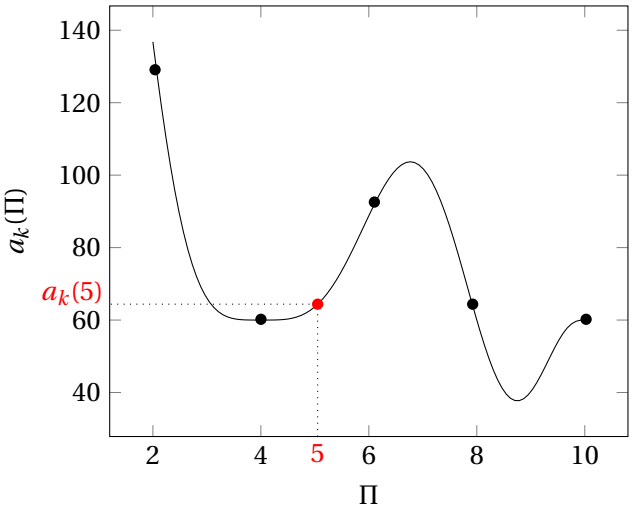

Figure 10: Visualization of methodology for interpolation of POD coefficients.

The idea of the interpolation between modal coefficient in the POD snapshot interpolation method is to find values for coefficients that are not in the dataset, by cubic spline interpolation as describe above. Say that the set for dimensionless number Π is $\Pi = [2,4,6,8,10]$. We run POD algorithm as described in section 3.2.1, and get a set of POD coefficient. How large the set is depends on number of snapshots, but here we have 5 snapshots for each of the values Π, and therefore 5x5 POD coefficients. Say we want to find the modal coefficient for $\Pi_{int} = 5$, that is not in our original set, Π. Then we need to interpolate between all the given values in the set, and the depending modal coefficients for the Π in the domain. Then we get the modal coefficient, $a_k(\Pi_{int})$, for the value that's not in the set, see illustration figure 10.

The interpolation between modal coefficients was programmed in Python 3.6, and a snipped of the source code for interpolation can be seen in figure 11 for one iteration. This need to be done five times according to number of snapshots given.

```
from scipy import interpolate #Import package

def f(x): #Define a function
    x_points = [] #List of dimensionless numver values to interpolate between
    y_points = [] #Calculated POD modeal coefficients at each dimensionsless value

    tck1 = interpolate.splrep(x_points, y_points,s=0) #Store values at each point for correlation

    return interpolate.splev(x, tck1) #Interpolate between x and y points for new value x, given in funciton
```
Figure 11: Python code for implementation of interpolation method.

From description above, x-value in function $f(x)$ will be 5 in case above, the list x-points would be Π and y-points would be modal coefficients $a_k(\Pi)$, which was calculated by method in section 3.2.1. Then we can calculate new modal coefficient for Π_{int}. For this method implemented in Python, Cubic spline interpolation is default method when using interpolate.splev function.

3.2.3 Visualization of results from POD method

When it comes to presenting of visualization for the results from the POD-interpolation method, we used MATLAB for this purpose. After the steps of running the POD algorithm, doing interpolation of POD coefficients and then use equation (42) for creating POD dataset of unknown values for flow variable, we can finally visualize the results. This was done by doing Delaunay triangulation function in MATLAB, see figure 12. This method does triangulation of points in dataset, which means that it takes lines, joining a set of points together, so each points gets together to its nearest neighbour point.

```
%Extract data into array
T = T.data(:,1);
x = x.data(:,2);
y = y.data(:,3);

%Delaunay triangulation part, for coordinates x and y
tri = delaunay(x,y);

[r,c] = size(tri);
disp(r);

%Plotting part
g1 = figure(1);
h = trisurf(tri, x, y, T);
```

Figure 12: Matlab code for implementation of Delaunay triangulation

This method is used for all the visualization of POD and DV results in this thesis, and can be seen in all sections involving visualization, such as section 6.1.

3.2.4 Procedure scheme for use of POD snapshot interpolation method

This section summarizes the methodology of the POD-interpolation method. The steps shows how to use the POD snapshot interpolation method, based on all the previous descriptions, figure (13).

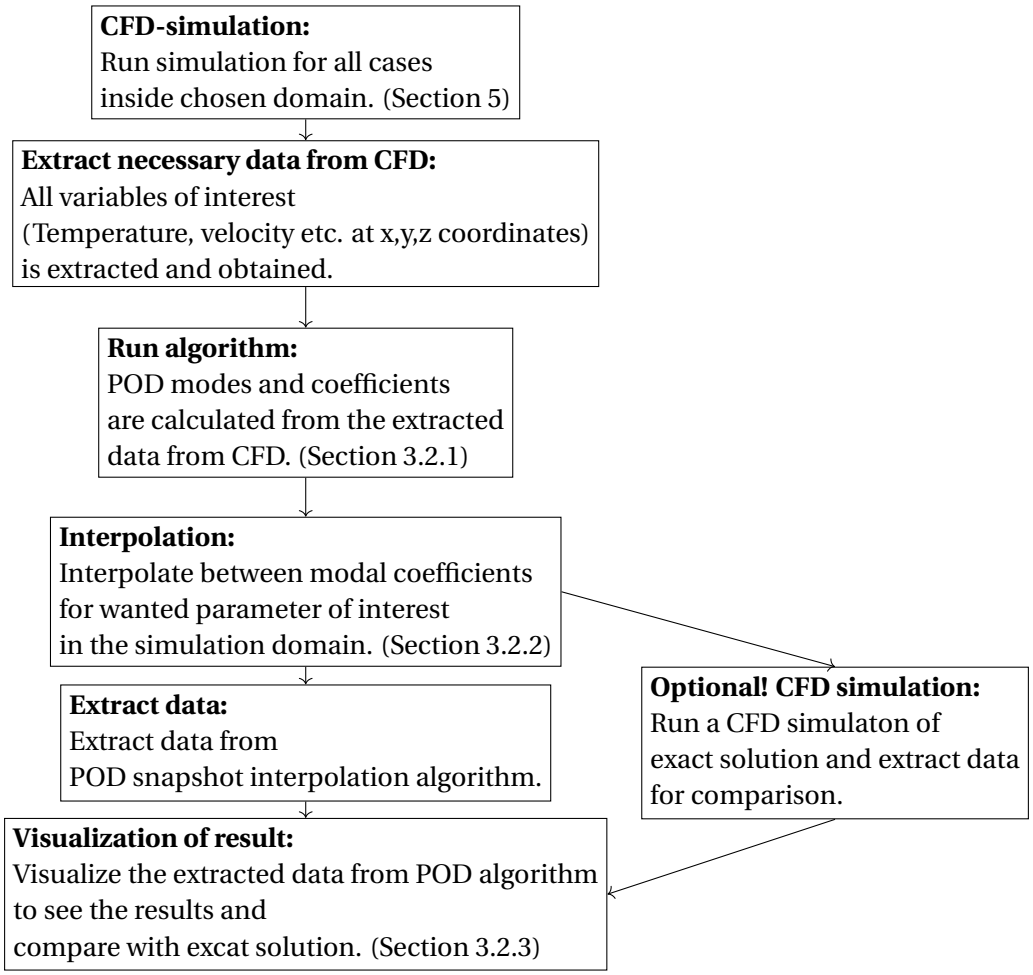

Figure 13: Description of steps from CFD through POD to visualization of results.

The idea of figure 13 is to give the reader an overview of how to perform the method presented in this thesis. Following the steps in the figure, and implement the necessary code should be sufficient to use POD snapshot interpolation method.

4 Validation case for POD snapshot algorithm

In order to have a validation case for this thesis, we have chosen a test problem involving similar kind of physics expected in a DV-system. This involve solving a problem with heat transfer and fluid flow with active gravity source term. The test case is similar to that presented by Aminossadati and Ghasemi [1] and Selimefendigil [25].

4.1 Validation case setup

This 2D benchmark test case consists of a steady laminar compressible flow through a horizontal channel with an open rectangular cavity in which a discrete hot surface is placed at the bottom wall of the cavity, see figure 14. The height of the heat source is set to $H/20$. At the inlet the velocity inlet boundary conditions is used with specified temperature (T_c) and velocity (u_{in}). The outlet are set as flow outlet with same mass flow value at the inlet with appropriate sign to ensure the global mass conservation. All walls are treated as insulated, except the heat source witch is set to a temperature (T_h).

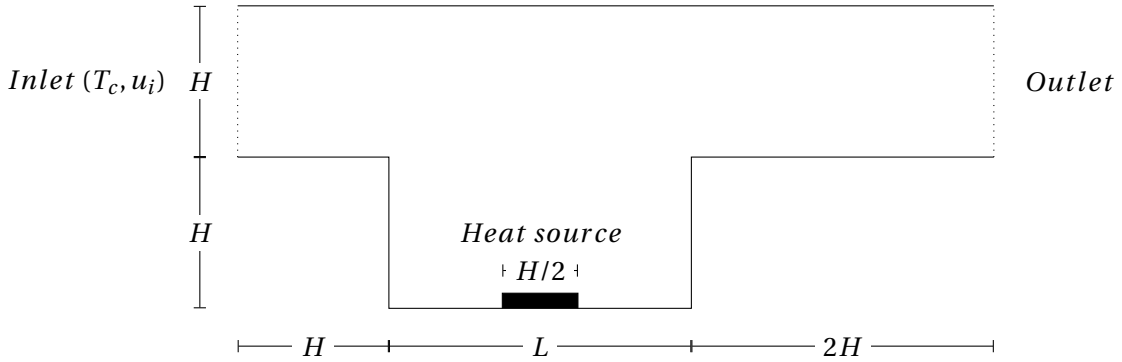

Figure 14: Modelsetup ($L = 2H$) for validation case by Aminossadati and Ghasemi [1].

A suitable 2D computational domain consisting of 5175 computational cells is used to simulate a case with Richardson number $Ri = 100$ where its defined as:

$$Ri = \frac{g\beta(T_h - T_c)H}{u_{in}^2} \tag{45}$$

Here, g is the acceleration due to gravity, β is thermal expansion coefficient, T_h is the temperature of the hot surface, T_c is the temperature at the inlet, H is the characteristic length (depth of the cavity) and u_{in} is the inlet velocity. Richardson number represents the importance of natural convection effects to forced convection. Laminar compressible segregated flow solver setup as mentioned before is used for CFD predictions. Converged solution is extracted once the residuals for all equations drops below 10^{-7}.

4.2 Results validation case

Figure 15 displays the temperature contour lines, and shows a very good agreement of the present solution with the previous studies reported by Aminossadati and Ghasemi [1] as well as Selimefendigil [25] using Boussinesq approximation. This indicates that the mesh is sufficient enough to be used for validation case for POD algorithm.

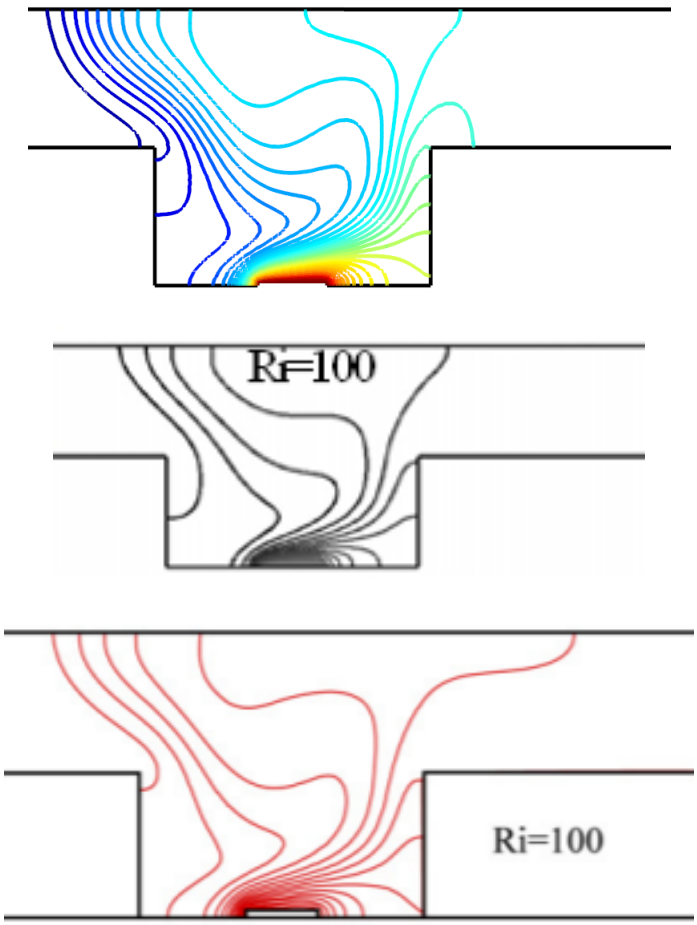

Figure 15: Comparison of numerical solutions, temperature contours for $Ri = 100$. top: present study, middle: Selimefendigil [25], bottom: Aminossadati and Ghasemi [1].

To verify the implementation of the overall POD methodology, steady state CFD solutions are performed with varying Ri, for a fixed value of Grashof number $Gr = 10^4$. The eight CFD solutions obtained via the same aforementioned convergence criteria for $Ri = 40, 50, 60, 70, 80, 90, 100$ and 110 are used as snapshots input data for the POD technique. The contours of the non-dimensional temperature was visualized by following formula:

$$\theta(Ri, \vec{x}) = \frac{(T - T_c)}{(T_h - T_c)} \tag{46}$$

As we can see in figure 16 with the increase of Ri the natural convection effects becomes dominant.

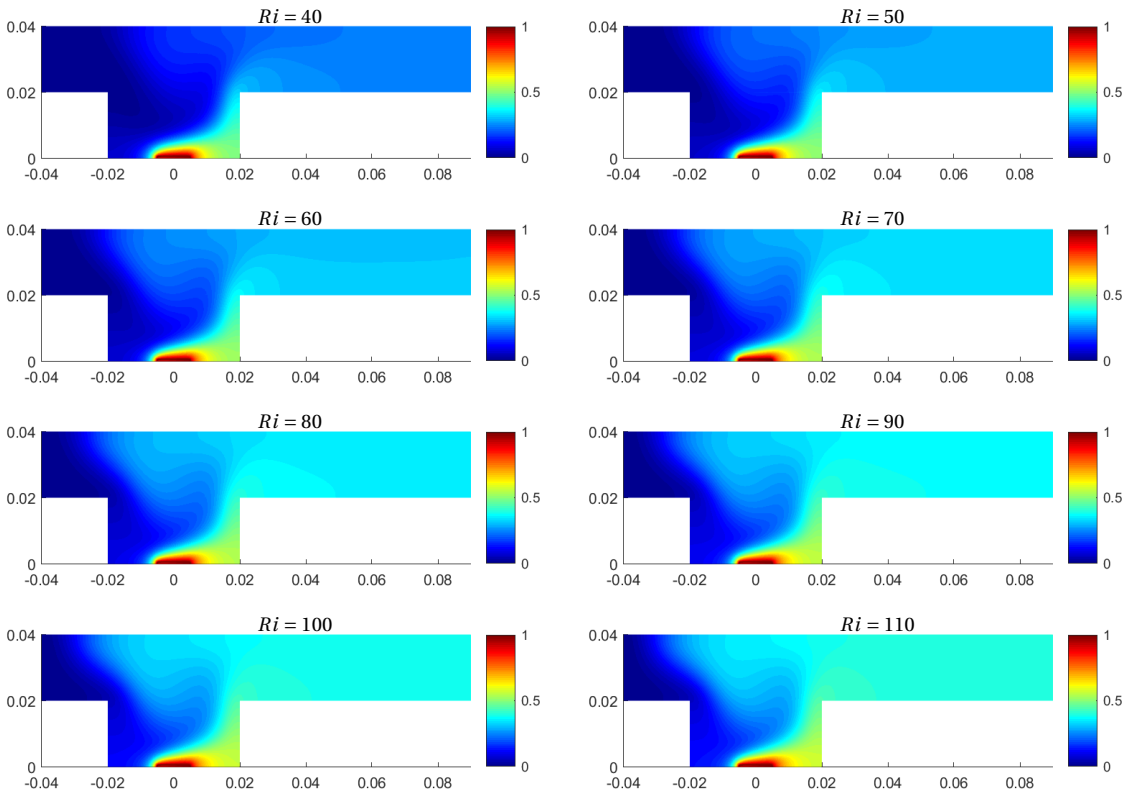

Figure 16: Contours for θ for all CFD-simulation cases for different Richardson numbers.

The POD-interpolated solution for $Ri = 75$ is constructed and compared with the actual CFD solution for verification and validation. Figure 17 clearly shows the reliability of the implementation. The error estimate is also low, and we can therefore clearly state that the implementation of algorithm is correct, and reproduction with POD interpolation gives good agreement with solution obtained from CFD simulation.

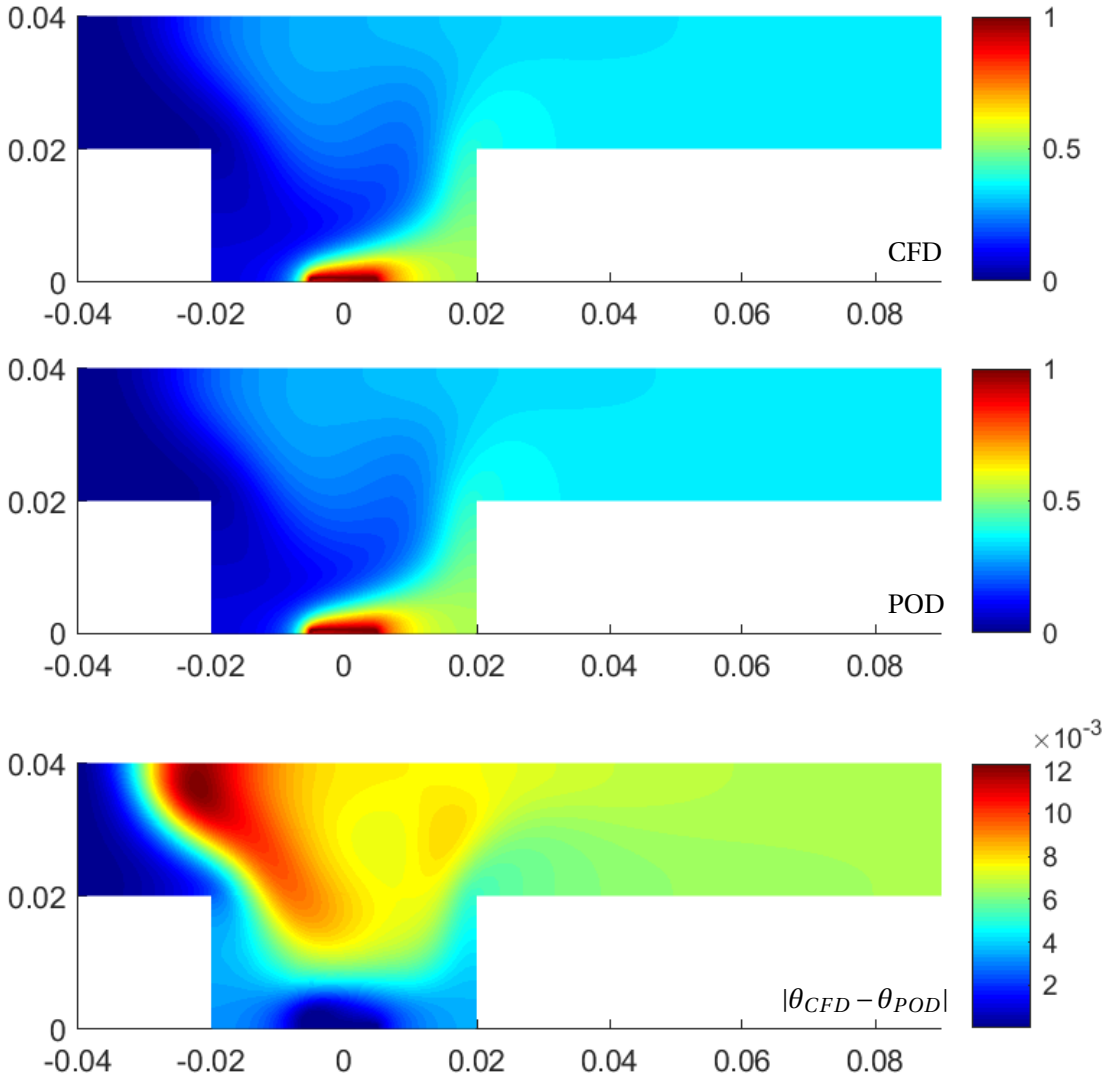

Figure 17: Comparison of CFD and POD predictions, contours of θ and error estimates for Ri=75.

The spatial structures of the POD modes are shown in Figure 18. The relative energy of the POD modes can be estimated from the eigenvalues by:

$$E_r = \frac{\lambda^i}{\sum_{i=1}^{m} \lambda^i} \tag{47}$$

Where λ^i's are the eigenvalues, (see equation (38)) when running the POD algorithm. The energy associated with the first POD mode is found to be 99.99999% and the rest of the modes assume values of the order of 10^{-7}% or less. This reveals that the most of the energy contained within the first POD mode, and therefore reconstruction with just on mode, will give a good approximation. We can also see from the spatial structures for Θ in figure 18, that main structure for all cases is quite similar to the first mode, which agrees with that most of energy is conserved in first mode.

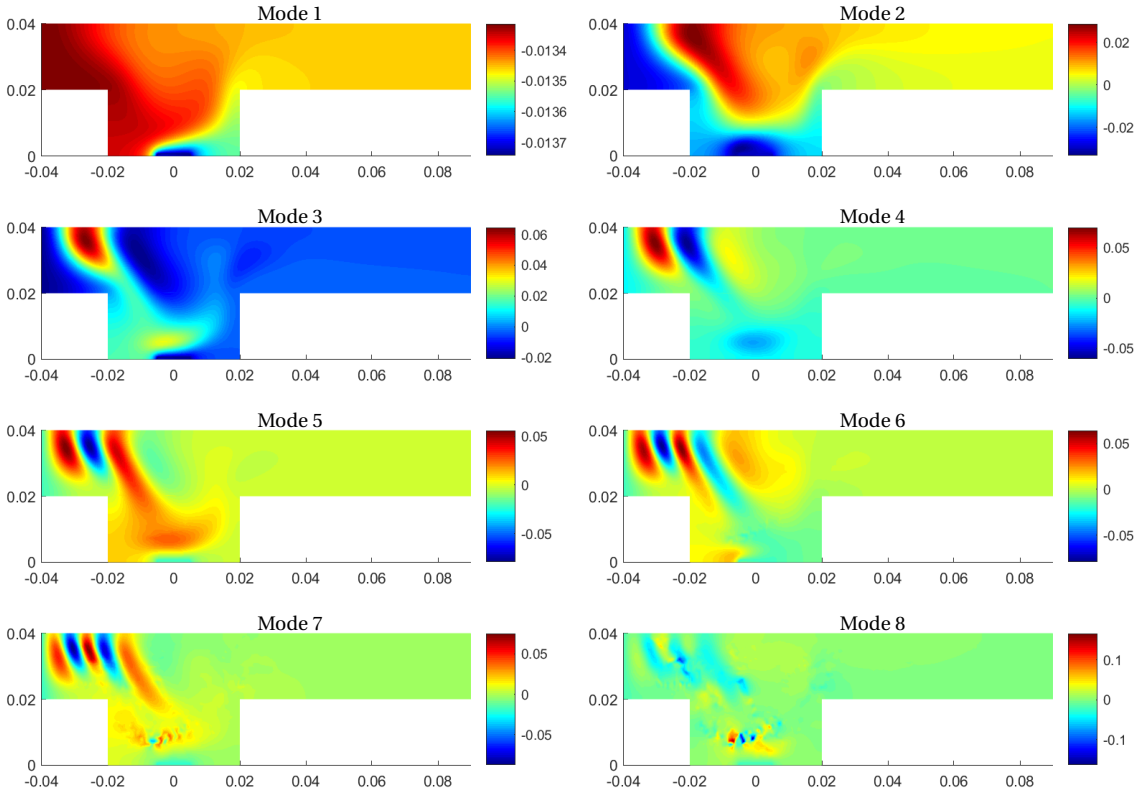

Figure 18: Spatial structures of the POD modes for θ.

5 CFD simulation of indoor air flow with DV-system

Here, we present the simulation of a DV-system in a room, and usage of POD based interpolation method for faster prediction of indoor air flows. The numerical setup is described and the model set up is been based on Nordtest [22] description of a DV setup. This is presented in the next section, followed by results and discussion for CFD simulation and POD interpolation method.

5.1 Setup for simulation

The box model of the room is 5.6 m x 2.8 m x 7.5 m (Length x height x width). The diffusers have a total area of 0.24 m^2 with height 0.3 m and the width 0.8 m. The heating wire along the wall, 0.7 m above the floor is supplying the heat into the room. See figure 19 for 3D visualization. [22]

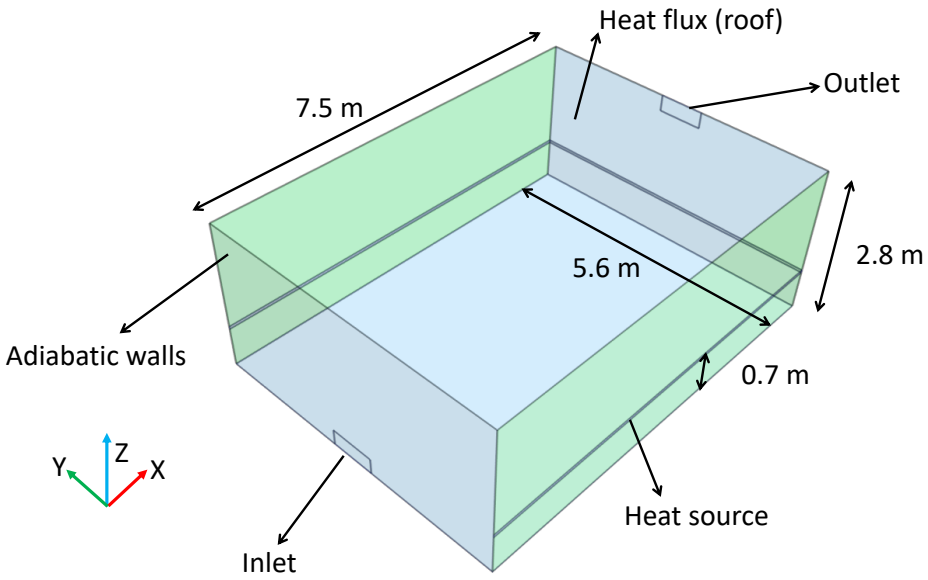

Figure 19: Computational setup of the indoor airflow study, domain sepsifications.

Mesh generation

Automated mesh in Star-CCM+ is used to generate the mesh. Trimmed mesher and prism layer mesher is used. Surface and volume control is used to make refined mesh in the main interaction zones the walls, inlet and the outlet. This is since the main physics of interaction would happen in these regions, and therefore a relatively coarser mesh was kept in the the center of the room. The volume control regions is called the refinement regions. 5 prism layers with a thickness of 0.05 is made near wall boundaries. A total of $\approx$ 1.06 million computational cells is used for the computations. Representation of the mesh can be seen in figure 20.

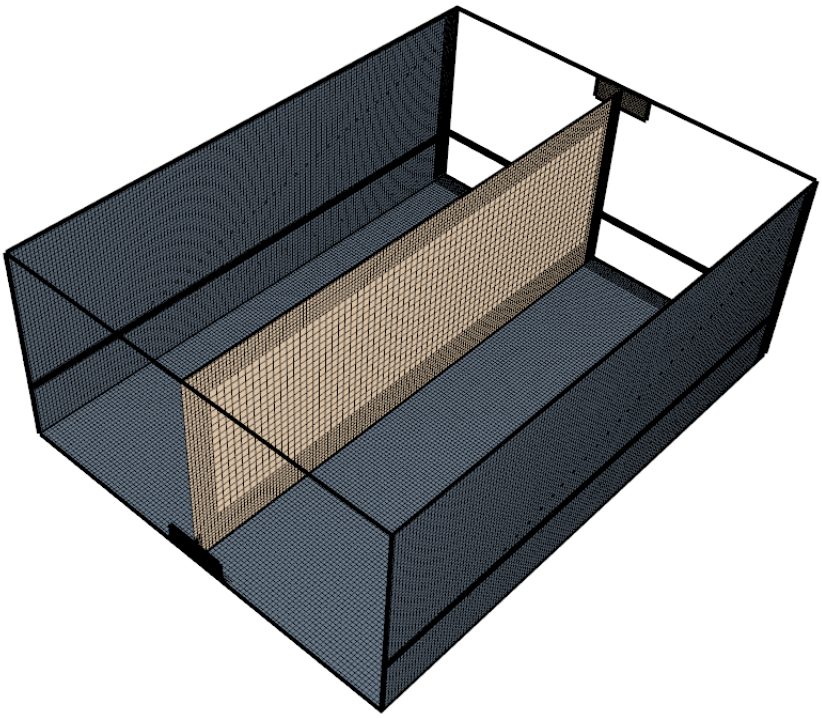

Figure 20: Computational setup of the indoor airflow study, mesh on some sample planes.

The near wall mesh resolution ensured that $0.02 < y^+ < 17.06$ for all cases. Note that the resolution near ceiling is $0.3 < y^+ < 6.4$ and near floor is $0.08 < y^+ < 6.2$ for all cases. Figure 21 shows wall y^+ for a simulation with $Ar = 2$.

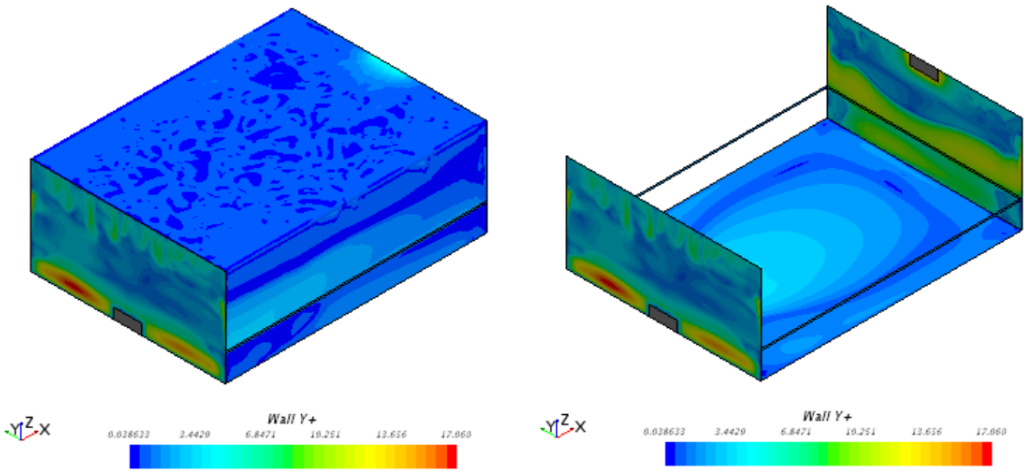

Figure 21: Presenting y^+wall values for $Ar = 2$.

Turbulence model

As described earlier on in the method section, the SST (Menter) $\kappa - \omega$ turbulence is used for the simulations of the DV-system.

The inlet boundary condition has been given values according to the k-ω turbulence model for specific dissipation rate (SDR), ω, and turbulent kinetic energy (TKE), k_0. These values changes for different mass flow at the inlet according following equations:

$$l_0 = h/10 \tag{48}$$

$$k_0 = 1.5(0.04 \cdot u_0)^2 \tag{49}$$

$$\omega = \frac{\epsilon}{k_0} = \frac{k_0^{1.5}}{k_0 l_0} = \frac{k_0^{0.5}}{l_0} \tag{50}$$

Where l_0 is some length scale, h is the height of the inlet and u_0 is velocity at the inlet calculated from the mass flow at the inlet [28, p. 77 and p. 90]. The values usd for the different cases can be seen in table 1:

Table 1: Overview of turbulent kinetic energy and specific dissipation rate for each simulation.

	TKE, k_0 $[m^2/s^2]$	SPR, ω [1/s]
$Ar_1 = 2$	4.33E-4	6.94E-1
$Ar_2 = 6$	2.08E-4	4.81E-1
$Ar_3 = 10$	1.48E-4	4.06E-1
$Ar_4 = 14$	1.18E-4	3.63E-1
$Ar_5 = 18$	1.00E-4	3.34E-1
$Ar_6 = 22$	8.76E-5	3.12E-1
$Ar_7 = 26$	7.83E-5	2.95E-1
$Ar_8 = 30$	7.12E-5	2.81E-1
$Ar = 7$	1.88E-4	4.57E-1
$Ar = 15$	1.13E-4	3.54E-1

At the outlet boundary, condition is set to have zero gradient for both turbulent kinetic energy and specific dissipation rate.

Physical model

Steady 3D simulations are performed. Ideal gas for air is used as the fluid, with the coupled flow solver. Gravity is used and the all y^+ treatment. Second order scheme is used for the coupled flow solver. Converged solutions for all cases are extracted once the residual for mass conservation stabilise at $\approx 4\times10^{-3}$, energy conservation stabilises $\approx 8\times10^{-4}$, Z-momentum stabilise at $\approx 1\times10^{-4}$ and residuals for all remaining equations drops below 4×10^{-5}. Figure 22 shows the behavior of the residuals for a sample case.

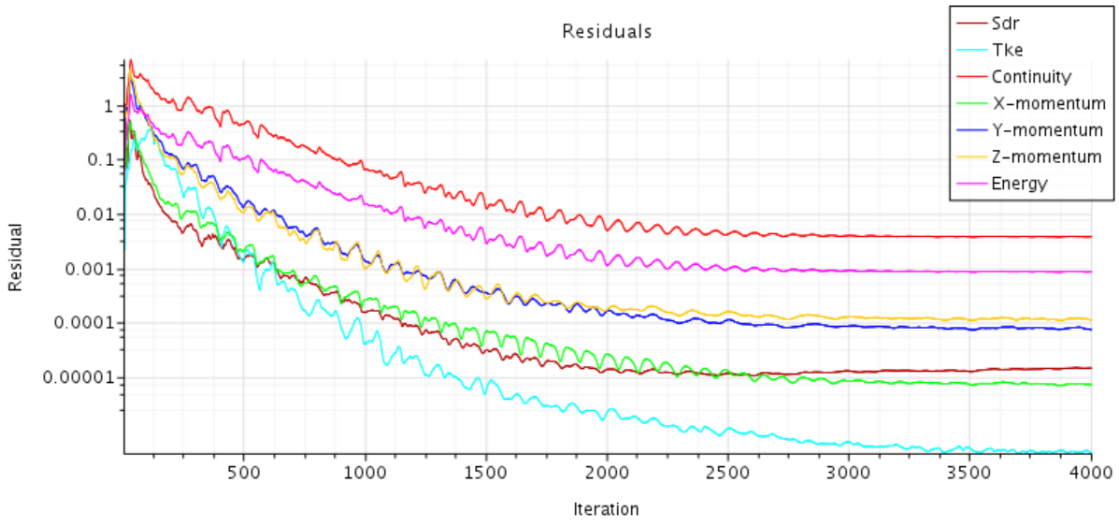

Figure 22: Typical residual for all simulation cases. Image is residuals for simulation of $Ar = 2$.

Gravity

Boussinesq approximation has not been used, which is a method that gives no variation of density in the flow field, but the full gravity term. Therefore there is no simplifications in the governing equations, and the simulations is therefore more realistic to the physical world.

Boundary conditions

The boundary conditions are summed up in figure 19 and in a list below:

- **Inlet:** Mass flow inlet condition is used. Since the flow is simulated as compressible, mass flow is preferred instead of velocity inlet. One of the reasons is when having velocity inlet the mass flow will change due to different density at the inlet. For cases as ventilation, where constant mass flow in is expected, mass flow inlet is preferred. A standard inlet temperature for DV-systems, $T_{in} = 17°C$ was used, and a density of $\rho_{in} = 1.216\ kg/m^3$.
- **Outlet:** The exhaust conditions are set as flow outlet with same mass flow value at the inlet with appropriate sign to ensure the global mass conservation. Zero gradient for temperature, specific kinetic energy and turbulent kinetic energy was applied.
- **Walls:** The walls was set to have no-slip condition and was adiabatic.
- **Heat source:** The wires had a thermal specification as heat source. Their was set to give constant supply of total heat according to the table 2, where a total of 120 W was supplied, acting as the heat supplied from one human.
- **Roof:** The roof was set to have a heat loss of 1 W/m^2 as described in Nordtest [22].

5.2 Test cases for CFD simulations and domain for POD snapshot method

Table 2 summarises the test cases for different Archimedes numbers where POD based interpolation is going to be used. The values are chosen on the background of having equally distance between the values, and all values are above $Ar > 1$ to hopefully achieve thermal stratification.

Table 2: Parameters of interest and their test domain.

	Ar_1	Ar_2	Ar_3	Ar_4	Ar_5	Ar_6	Ar_7	Ar_8
$q_{t,1} = 120$ W	2	6	10	14	18	22	26	30

Equation (29) is used to calculate the input parameters depending on Archimedes number in the CFD model. For POD method, we are interested to run algorithm for values other then in table 2, which was chosen to be $Ar = 7$ and $Ar = 15$. Further analysis is presented in these next sections.

6 Results and discussion

The flow physics involved in the present ventilation setup is governed by the Archimedes number (analogous to Richardson number as in validation case). Eight different test cases are simulated, (see table 2), as variable parameter leading to the following functional form for any non-dimensional flow variable, $\phi^*(Ar, \vec{x})$. The following analysis is based on the non-dimensional variables:

$$\rho^* = \frac{\rho}{\rho_{in}} \tag{51}$$

$$U^* = \frac{u}{u_{in}} \tag{52}$$

$$T^* = \frac{(T - T_{in})\ \rho_{in} c_p \dot{V}_{in}}{q_t} \tag{53}$$

where $\dot{V}_{in}$ is the volumetric flow rate at the inlet, c_p is the heat capacity at constant pressure, q_t is the total heat gain in the room, A_s is the diffuser area of inlet and L is the characteristic length that can be defined as the difference between the room height and height of the diffuser. We first present the CFD solutions for different Archimedes numbers. Subsequently, the analysis of POD-interpolated solutions for $Ar = 7$ and $Ar = 15$ are presented in the non-dimensional form for each parameter $T^*(Ar, \vec{x})$, $U^*(Ar, \vec{x})$ and $\rho^*(Ar, \vec{x})$ in different planes with an error estimate by:

$$Error = |(\phi^*_{CFD} - \phi^*_{POD})| \tag{54}$$

Then we will present spatial structures of POD modes and energy conserved in the modes.

6.1 DV characteristics and CFD snapshots

The Ar is varied essentially setting different inlet air supply velocity with fixed supply T_{in}, ρ_{in} and heat loads. As mentioned earlier, equation (29) is used as formula for Archimedes number. Figure 23 shows the distribution of U^* on a $x-y$ plane at z=0.1m. The typical air flow pattern for low air velocity diffuser in DV configuration involving the acceleration region (near field) and the velocity decay region (far field) can be clearly realised from the U^* contours. With increasing Ar, the maximum value occurs at further upstream (x-coordinate) locations. Evidently, the acceleration zone is larger for low Ar. For lower Archimedes number (e.g $Ar = 2$), we can see that higher values of U^* occur further away from the diffuser compared to the higher Archimedes numbers (e.g $Ar = 30$), figure 23. This is due to higher momentum from the inlet diffuser.

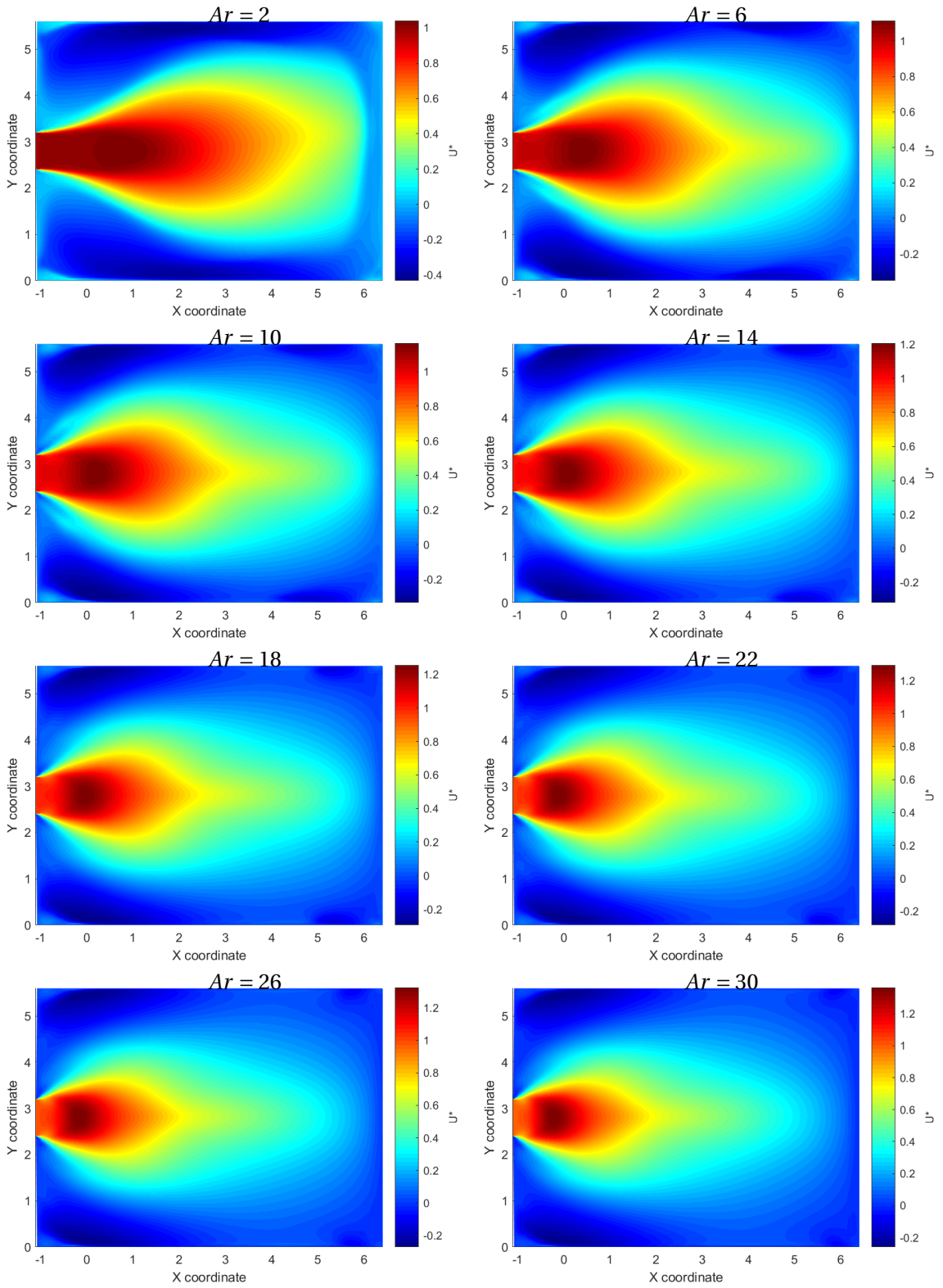

Figure 23: Contours of u-component of the velocity on a horizontal plane at 0.1 m above the floor for different Ar.

From the earlier statement it can be seen that (figure 24) for higher Archimedes number max velocity occurs on further upstream x-coordinate at $z = 0.1\ m$. For higher Archimedes number, we can also see that we will achieve a higher max velocity relative to the inlet velocity.

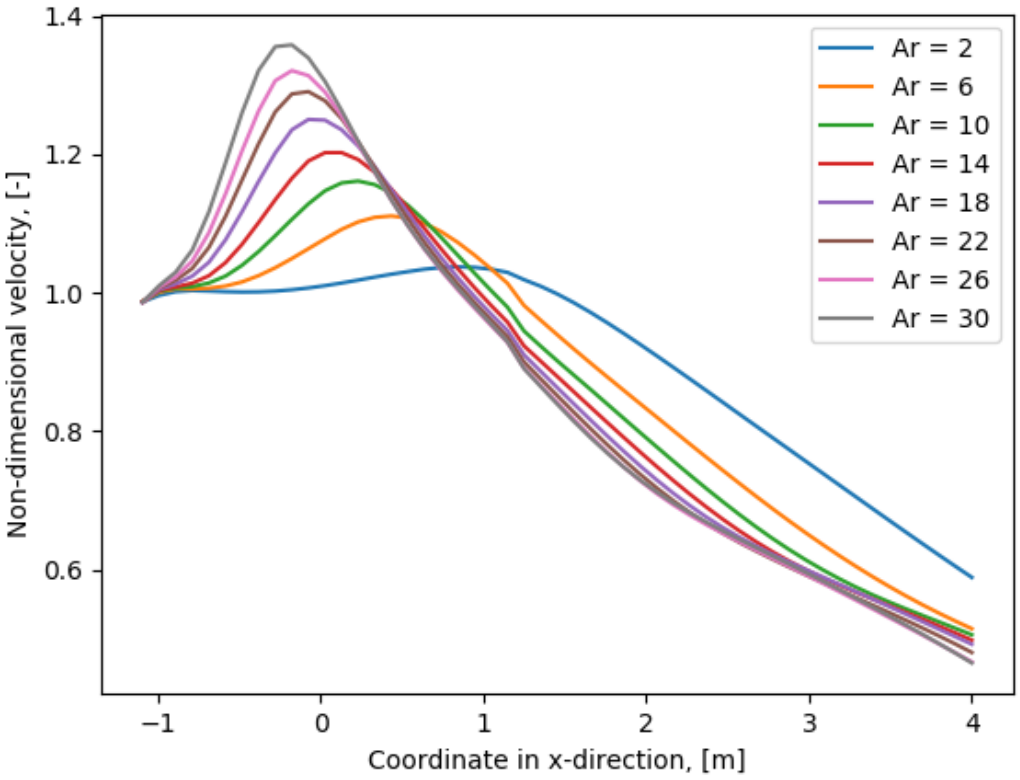

Figure 24: Plot of velocity u-component in the refinement region $z = 0.1\ m$ in middle of room.

We made contours of the non-dimensional velocity in the vertical plane, see figure 25. We can see that the establishment zone and acceleration zone are farther away downstream for lower Archimedes number. Max velocity occurs at some distance from the diffuser, so as stated in introduction section for DV-systems, (see section 1.1), the max velocity will occur further from diffuser. We can also clearly see that the flow goes further into the room for lower Archimedes number. The difference between max velocity and inlet velocity increase with increasing Archimedes number. At the outlet we can see some higher velocities, this is due to the outlet B.C and there is a under pressure at the outlet.

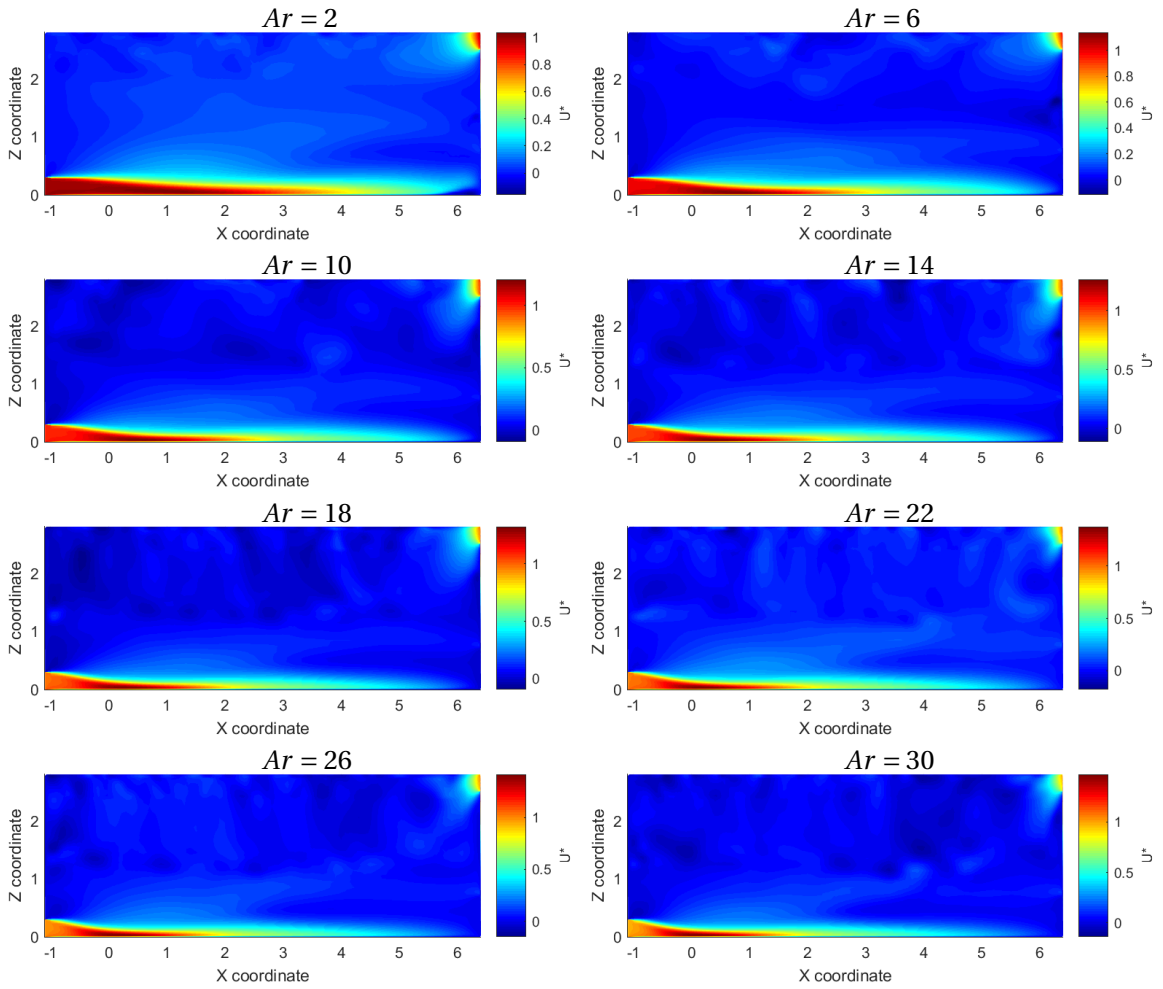

Figure 25: Contours of velocity on a vertical plane in the middle of the room at $y = 2.8m$ for different Ar.

Figure 26 shows the effective thermal stratification on a $x-z$ plane at the middle of the room ($y = 2.8\ m$) for all cases which is the key aspect of achieving the good air quality for a DV-system.

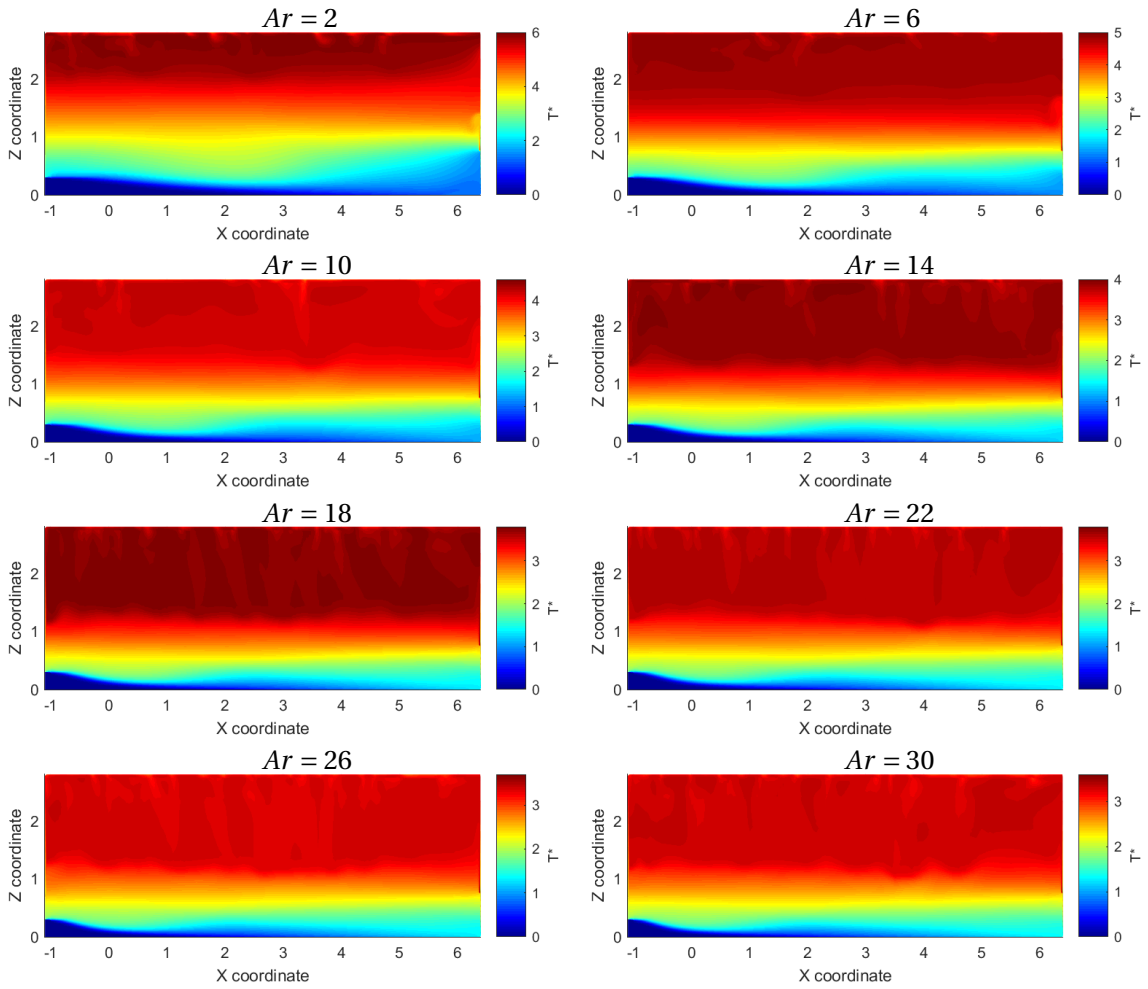

Figure 26: Contours of temperature on a vertical plane in the middle of the room at $y = 2.8m$ for different Ar.

We can see from figure 27 that for higher Archimedes number, we get lower temperature at the roof. Where also the plot of thermal stratification, figure 27, indicates the same. Good stratification is needed for a DV-system to remove the contamination in the room, and for $Ar > 1$ this is clearly achieved for this kind of room structure.

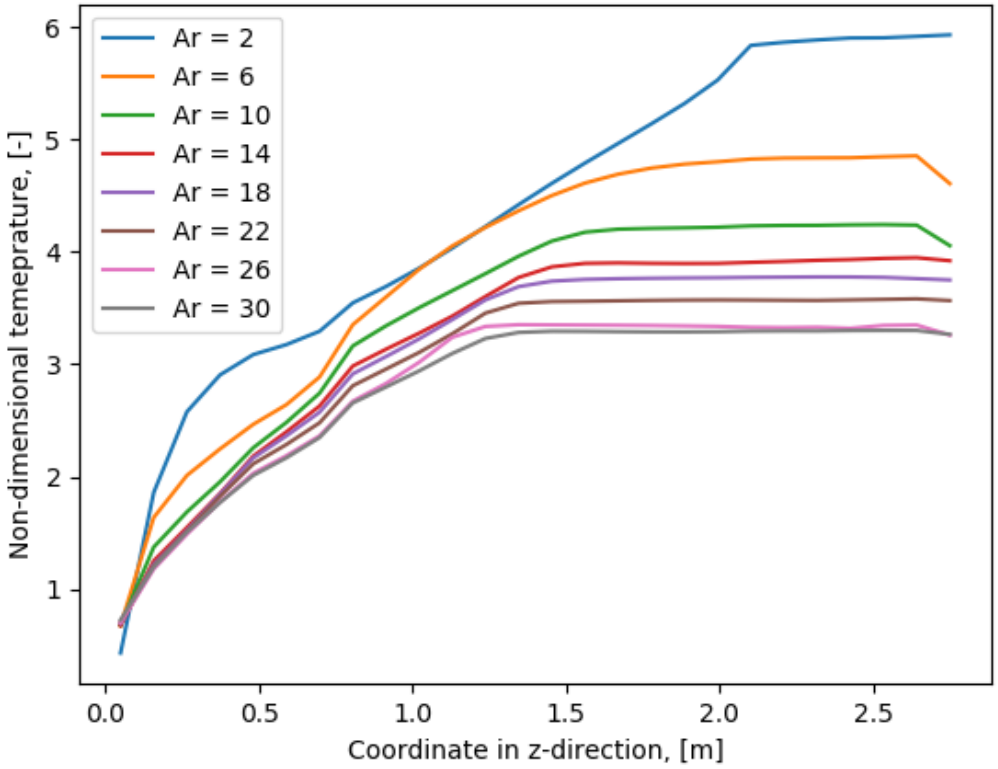

Figure 27: Plot of temperature along line probe at $x = 2.0$ m in middle of room.

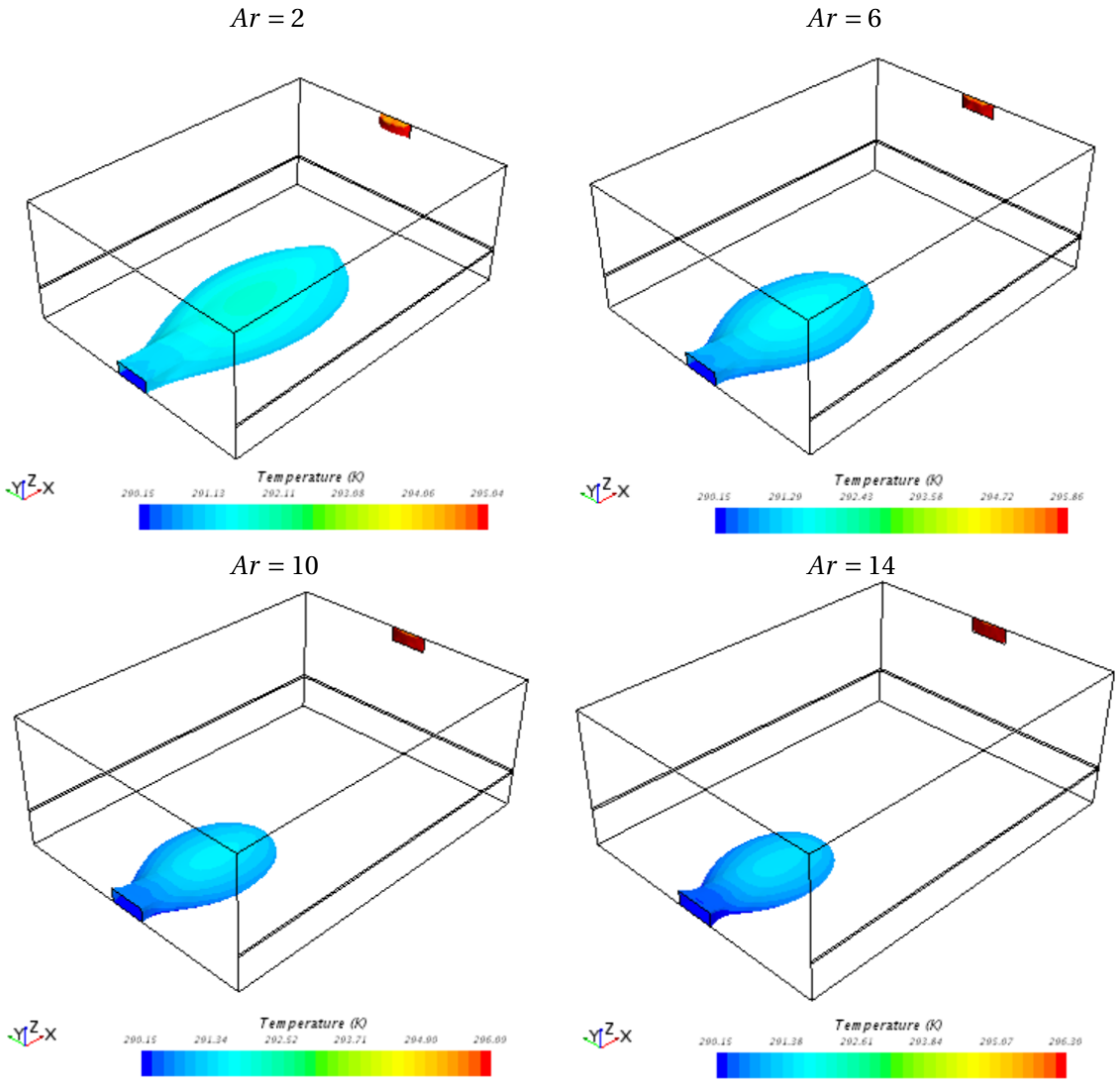

Figure 28: Isosurfaces at the inlet diffuser for four first Archimedes numbers.

Figure 28 shows the isosurfaces for velocity u-component with isovalue 0.2 m/s for four different Archimedes numbers, colored with temperature contours.These iso-surfaces shows that, lower Archimedes numbers have further penetration into the room than higher Archimedes numbers.

6.2 Nordtest method comparison

As introduced in section 2.5.4, Archimedes number has different forms and how DV-systems can be engineered. In this section we are presenting comparison between Archimedes number used in this thesis and Nordtest Archimedes number, and presentation of max velocity for all Archimedes numbers.

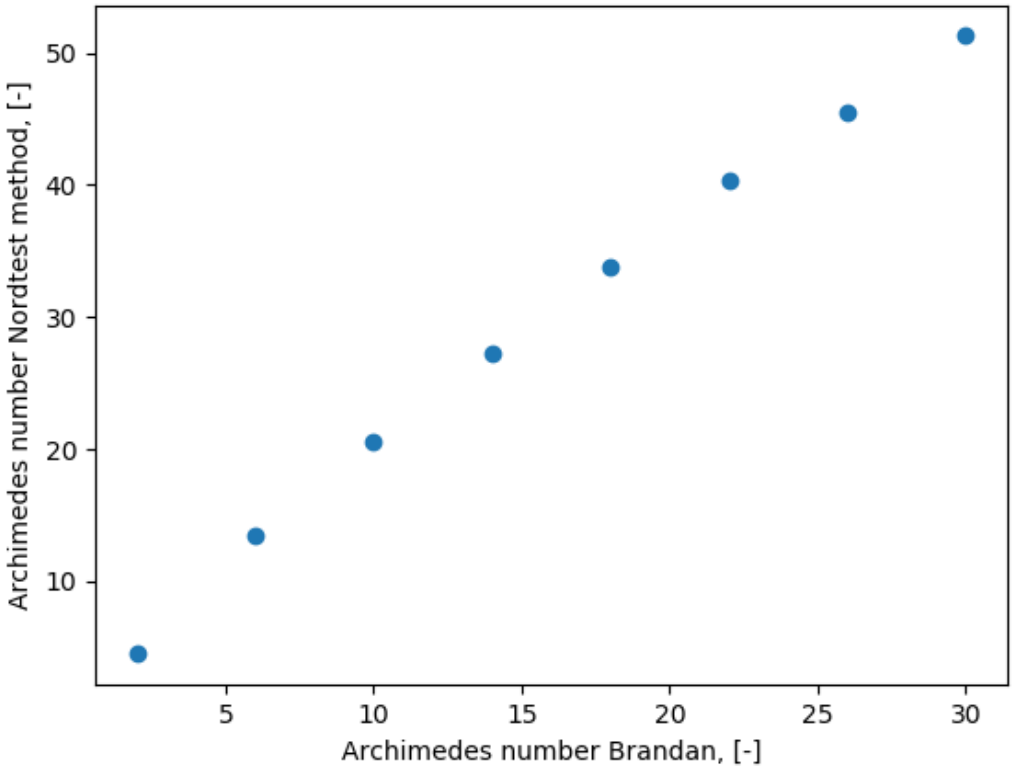

Figure 29: Comparison between Archimedes number proposed in Nordtest [22] and the on by Menchaca Brandan [17] in a scatter plot.

In figure 29, we show a scatter plot of the proposed Archimedes number from Nordtest method and the Archimedes number from Menchaca Brandan [17]. The Archimedes number from Nordtest method is calculated according to equation (31) in section 2.5.4. This is done by making a horizontal plane, 1.1 m above the floor with a 2 m distance from the diffuser according to the standard, and take the average of the temperature in this plane to get the reference temperature, T_r. The Archimedes numbers from Menchaca Brandan [17] is used in the simulation of the DV cases. We can clearly see that the Archimedes number from Nordtest method and Menchaca Brandan [17] is positively correlated, but the Nordtest method gives a higher value for the Archimedes number. The curve fitting function for scatter plot in figure 29 gotten from polynomial fit from Python is:

$$f(x) = -0.014x^2 + 2.107x + 0.753 \tag{55}$$

There could be of interest to take equation (30), and change it to see what the error would be for max velocity, v_{max}, changing the Nordtest Archimedes, $Ar_{Nordtest}$, with Menchaca Brandan [17]

Archimedes number, $Ar_{Brandan}$, such as:

$$v_{max} \approx k_{1,max} \cdot (Ar_{Brandan})^{k_{2,max}} \cdot B \tag{56}$$

Further on the max velocity in the middle of room at $y = 2.8$ for all simulations is presented, see figure 30.

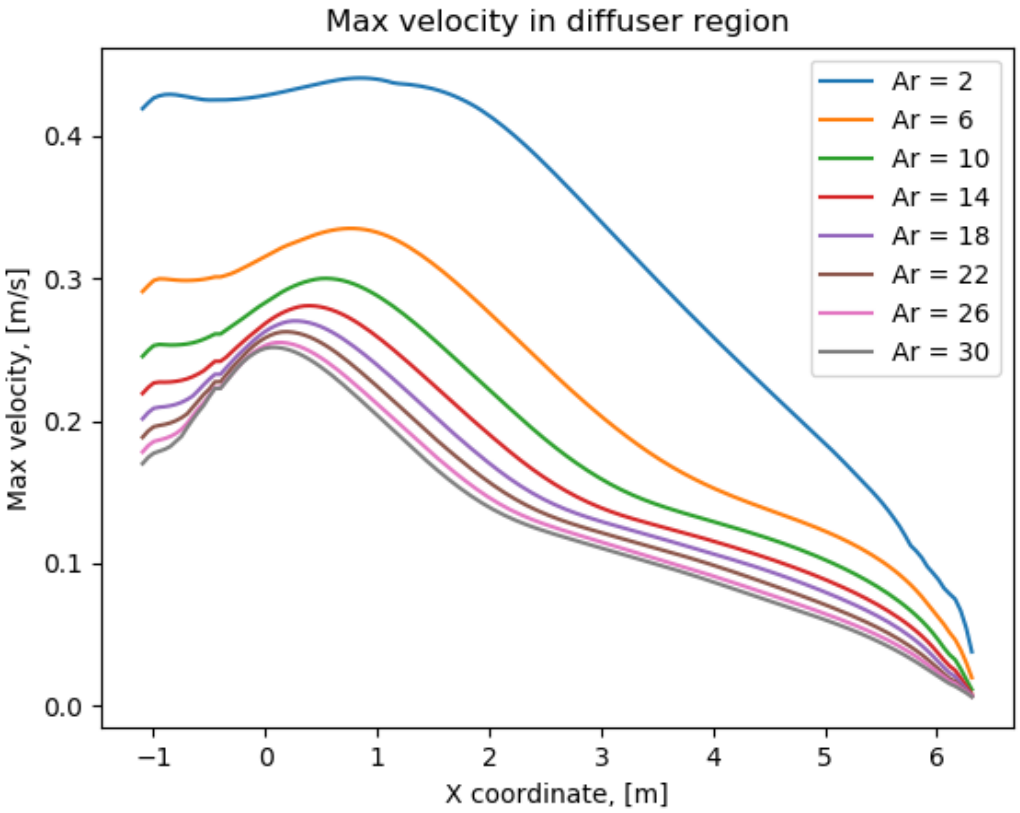

Figure 30: Max velocity for a plane in middle of room at $y = 2.8m$.

We can clearly see that difference between inlet velocity and max velocity in diffuser regions increase with increasing Archimedes number.

Since this method for analysis of the coefficients in the Nordtest method needs a lot of datapoints, the POD-interpolation method could be a great way to attack these kind of parametric studies. In the next section the results from POD-interpolation method is presented, and the accuracy is discussed.

6.3 Analysis of POD-interpolated prediction

For POD-interpolation prediction, 8 different snapshots is extracted from steady-state CFD simulation of DV-system, see table 2. We estimate the flow parameters for $Ar = 7$ and $Ar = 15$ via POD-interpolated methodology on two different planes, as shown in section 6.1, inside the refinement regions, since here the most complex fluid flow structures occur. The predicted contours of U^*, T^* and ρ^* at $x-y$ plane are compared with the actual CFD, which is presented below.

6.3.1 POD-interpolation prediction for $Ar = 7$

Below we present visualisation comparison between CFD and POD based prediction for $Ar = 7$.

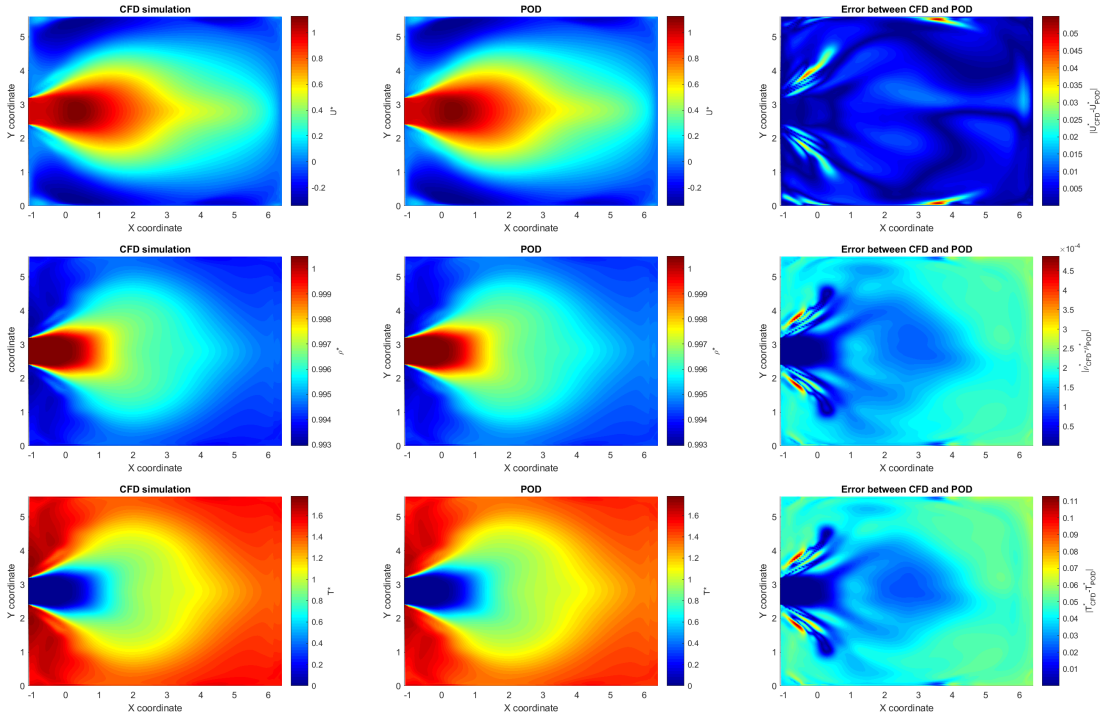

Figure 31: Velocity, density, temperature and error distributions on horizontal plane at 0.1 m above floor for $Ar = 7$.

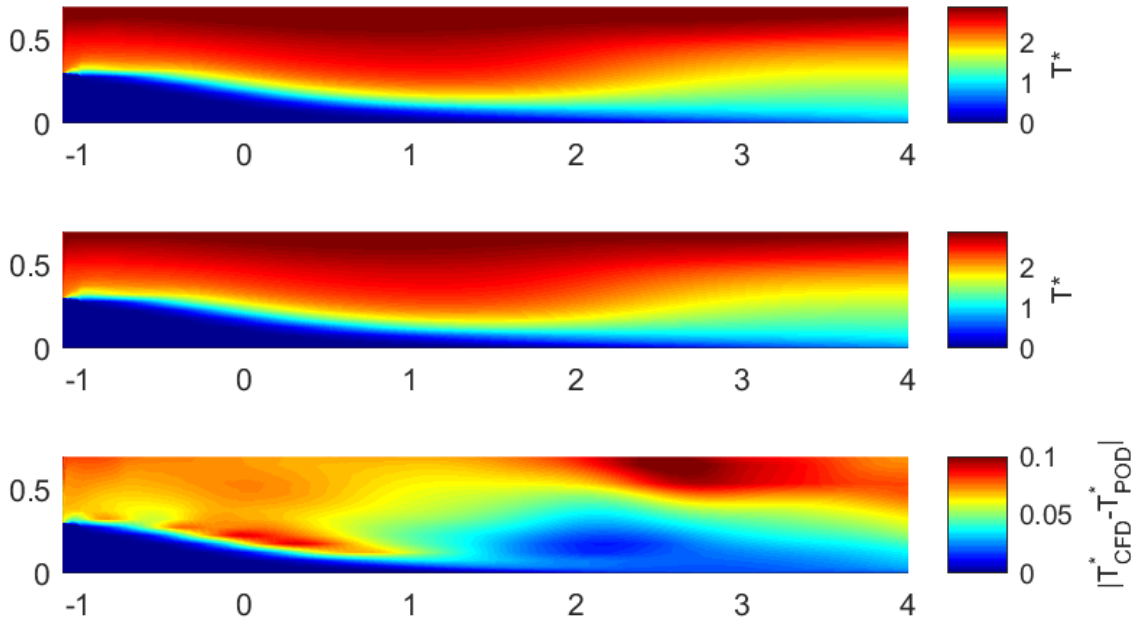

Figure 32: CFD, POD and error estimates on a vertical plane for T^* at $y = 2.8$ for $Ar = 7$. Top: CFD, middle: POD, bottom: Error estimate.

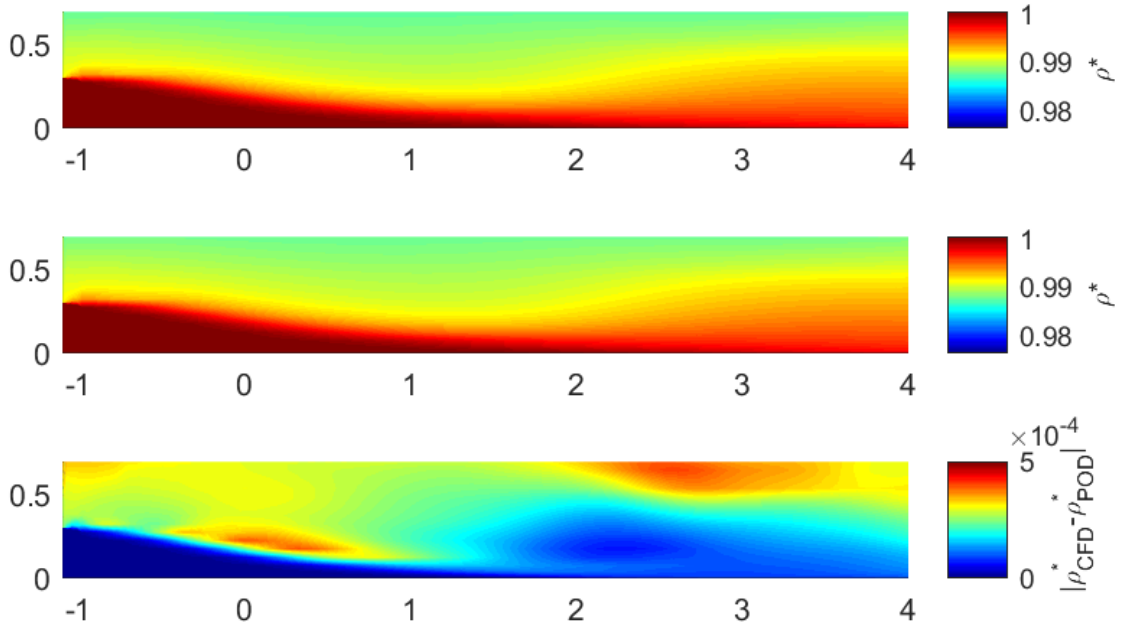

Figure 33: CFD, POD and error estimates on a vertical plane for ρ^* at $y = 2.8$ for $Ar = 7$. Top: CFD, middle: POD, bottom: Error estimate.

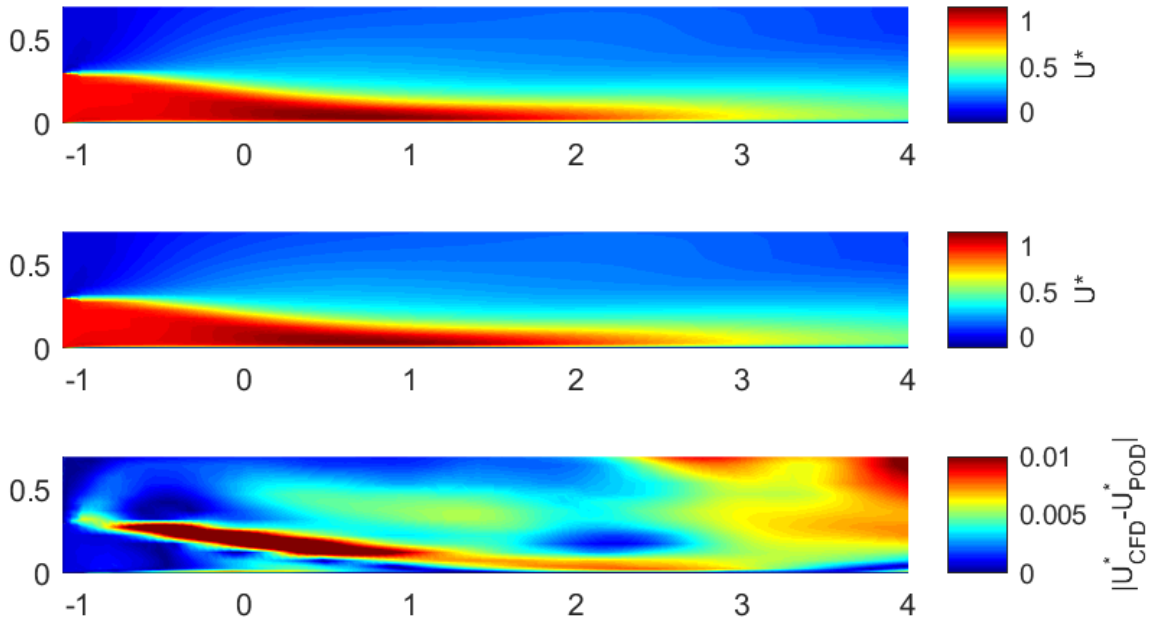

Figure 34: CFD, POD and error estimates on a vertical plane for U^* at $y = 2.8$ for $Ar = 7$. Top: CFD, middle: POD, bottom: Error estimate.

In figure 31, we first show the distribution of T^*, U^* and ρ^* in the horizontal plane. It can be clearly seen that the visualization with all modes, is almost identical as the CFD simulation results. The error estimate backs this up, where it shows a very small error between CFD and POD. One can see the similar trend in the vertical plane, (figure 32, 33 and 34), as in the horizontal plane, where the error estimate is low in the interaction region. It is evident that the error estimates for this plane appears relatively higher above the diffuser height levels having relatively coarser mesh in this region. Nevertheless, the errors are sufficiently low in the main interaction zone near and below the diffuser height level. The acceleration and velocity decay regions are predicted very well.

6.3.2 POD-interpolation prediction for $Ar = 15$

Here we present visualisation comparison between CFD and POD for $Ar = 15$. As in the last section for CFD compared with POD for $Ar = 7$, again one can see similar pattern of the results for $Ar = 15$. The error estimate is low between POD and CFD, and acceleration zone and velocity decay region is predicted really well as expected. See figure (35-38).

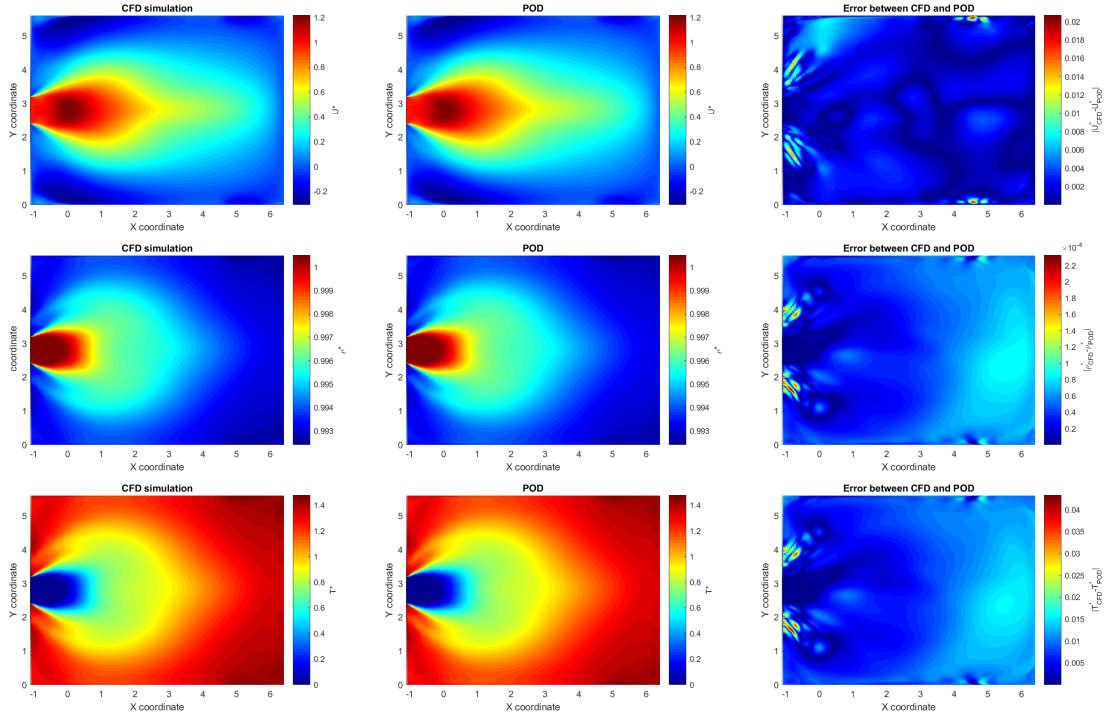

Figure 35: Velocity, density and temperature distributions on horizontal plane at 0.1 m above floor for $Ar = 15$.

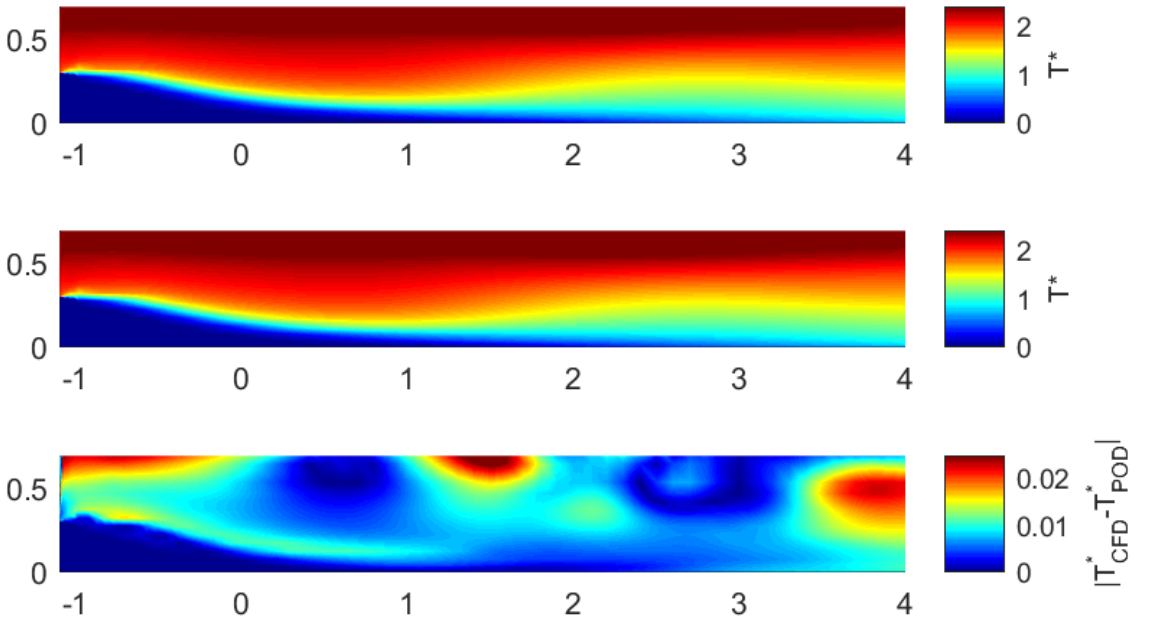

Figure 36: CFD, POD and error estimates on a vertical plane for T^* at $y = 2.8$ for $Ar = 15$. Top: CFD, middle: POD, bottom: Error estimate.

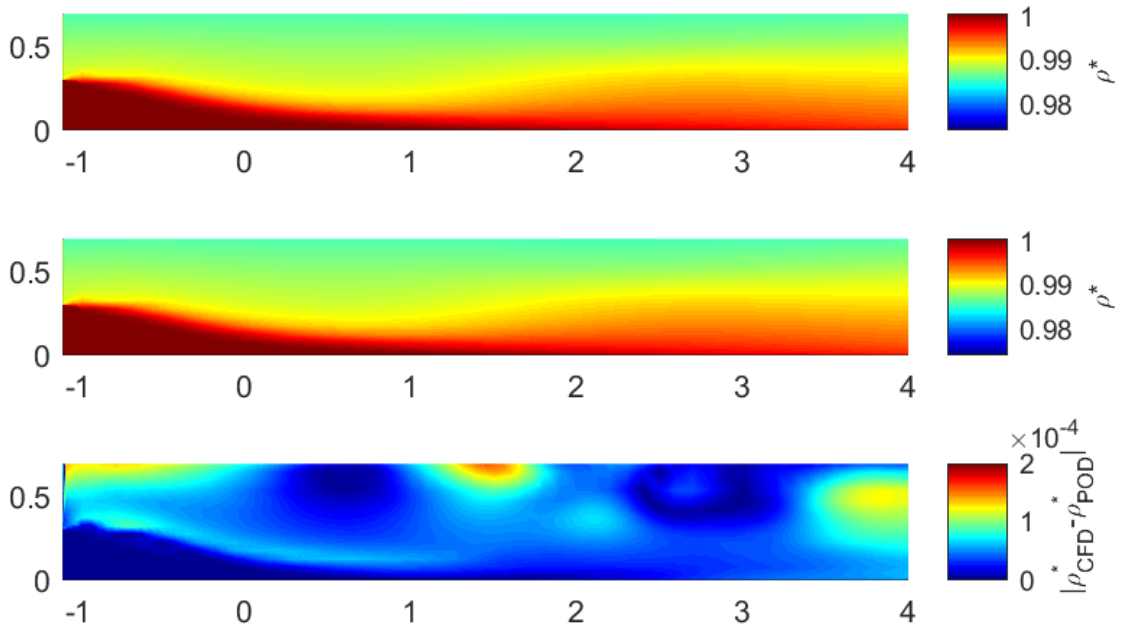

Figure 37: CFD, POD and error estimates on a vertical plane for ρ^* at $y = 2.8$ for $Ar = 15$. Top: CFD, middle: POD, bottom: Error estimate.

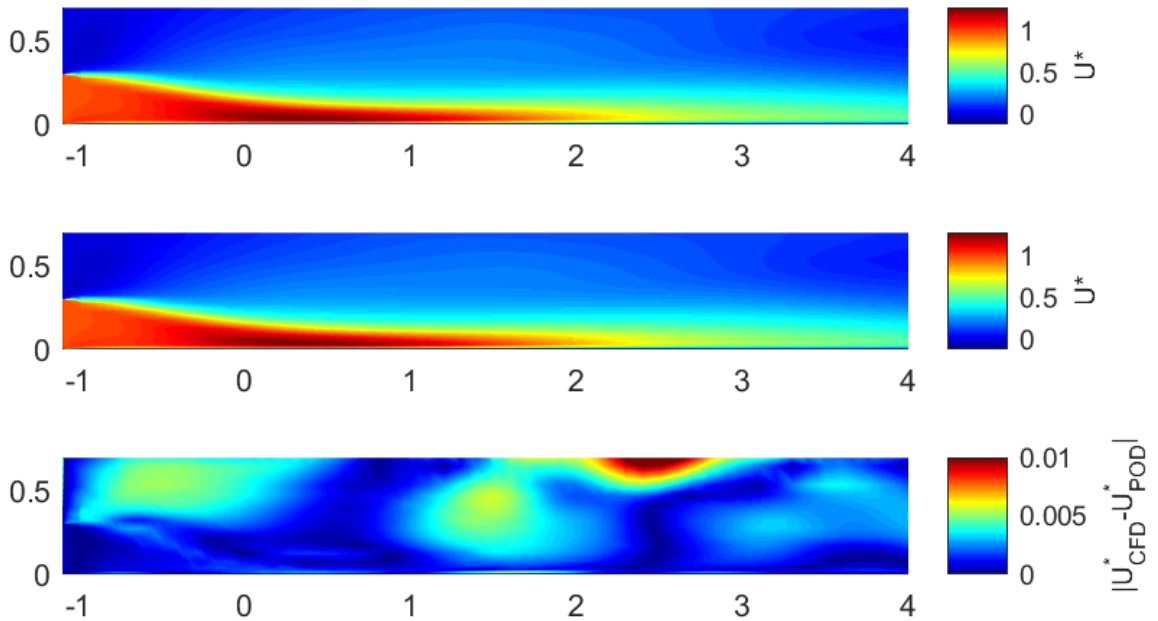

Figure 38: CFD, POD and error estimates on a vertical plane for U^* at $y = 2.8$ for $Ar = 15$. Top: CFD, middle: POD, bottom: Error estimate.

6.4 Spatial structures

The spatial structures are presented in this section for the 8 modes computed from the 8 snapshots in vertical and horizontal plane. The structures are computed from the U^*-component and we are interested in looking into how much of the energy that is captured in the modes. Figure 39 represents the modes in the horisontal plane and figure 40 in the vertical plane.

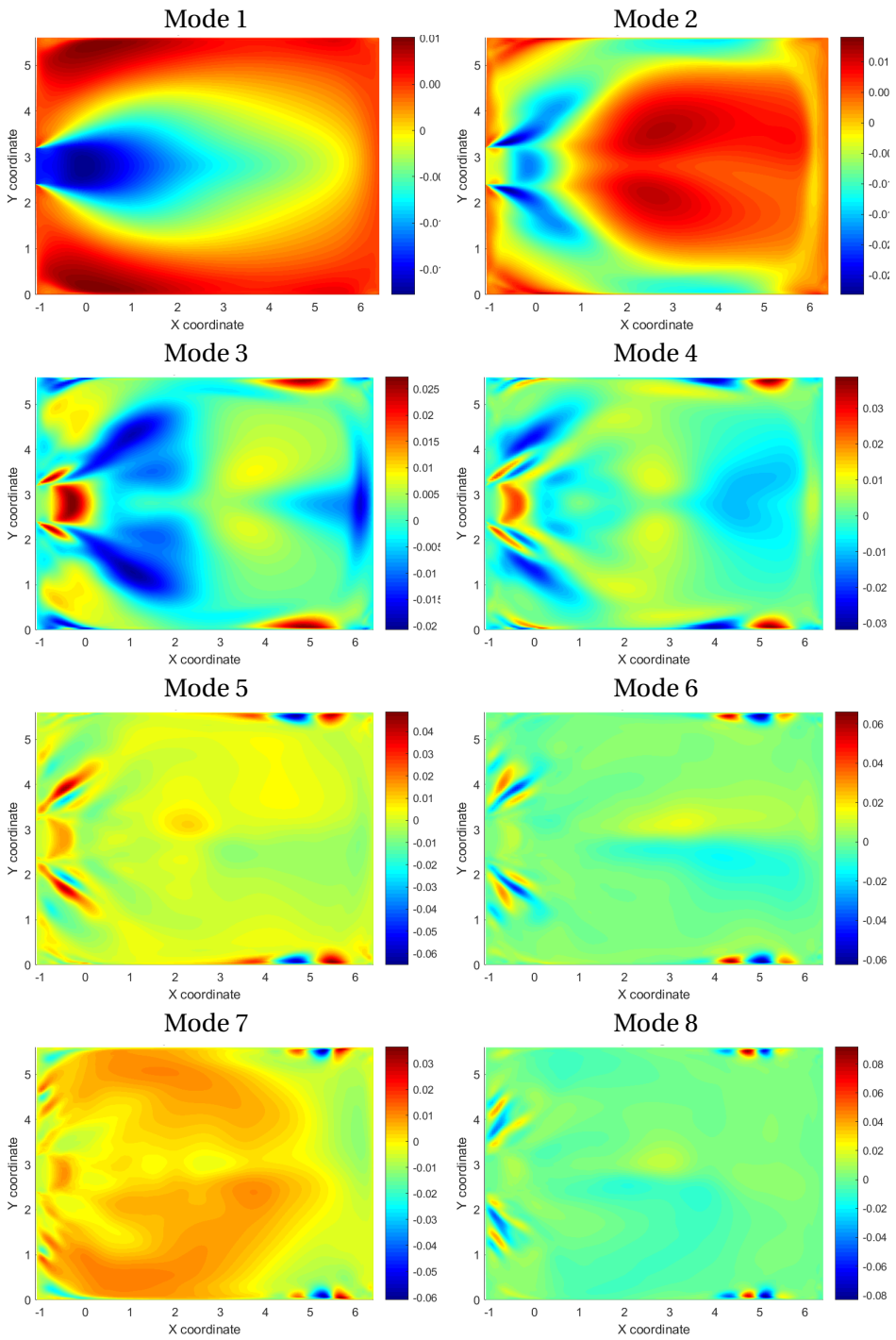

Figure 39: Spatial structures of the POD modes for u-component of the velocity field, x-y plane.

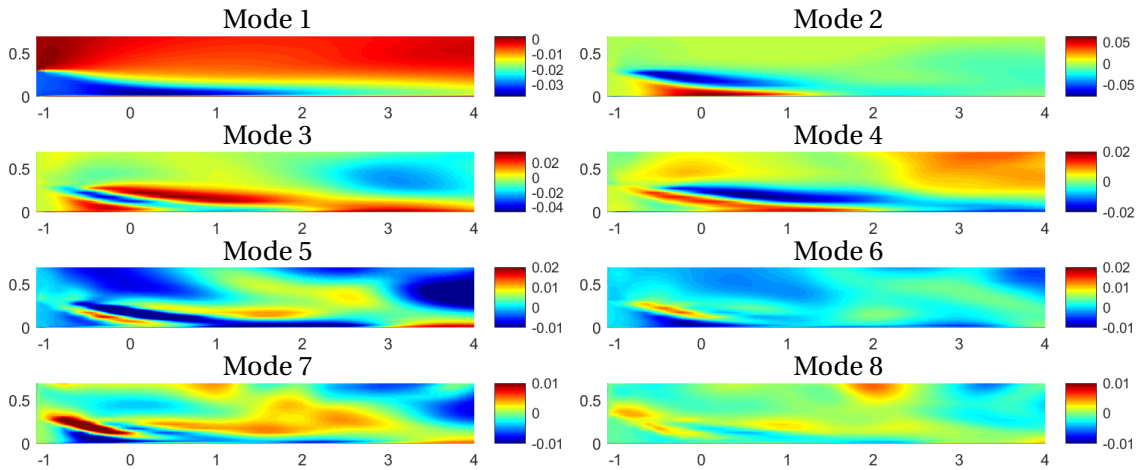

Figure 40: Spatial structures of the POD modes for u-component of the velocity field, x-z plane.

By comparing structures in figure 39 and 40, we clearly see that the first mode for both horizontal and vertical plane contains the most of the energy. The energy for the different modes are summarized in table 3, using equation (47).

Table 3: Energy catched by the modes in x-y and x-z plane.

	Energy x-y plane, [%]	Energy x-z plane, [%]
Mode 1	98.01	98.89
Mode 2	1.77	0.65
Mode 3	0.19	0.15
Mode 4	$2.24 \cdot 10^{-4}$	$7.70 \cdot 10^{-4}$
Mode 5	10^{-5}	$5.86 \cdot 10^{-4}$
Mode 6	10^{-5}	$5.07 \cdot 10^{-4}$
Mode 7	10^{-5}	$3.66 \cdot 10^{-4}$
Mode 8	10^{-6}	$2.85 \cdot 10^{-4}$

As we can see from table 3, the first two modes for both vertical and horizontal plane consist of more than 99.5 % of the energy. In the vertical plane, we notice that mode 4,5,6,7 and 8 are quite consistent with energy conservation in the value ine the range of 10^{-4} range. Since most of the energy is captured in the first two modes, good predictions of the flow in the DV-system can be acquired only by using the these two, which is shown in the next section.

6.4.1 POD-interpolation prediction for first two modes for $Ar = 7$

After looking into the spatial structures of the POD modes in section 6.4, it is interesting to investigate total error between POD prediction using all modes and using just two modes.

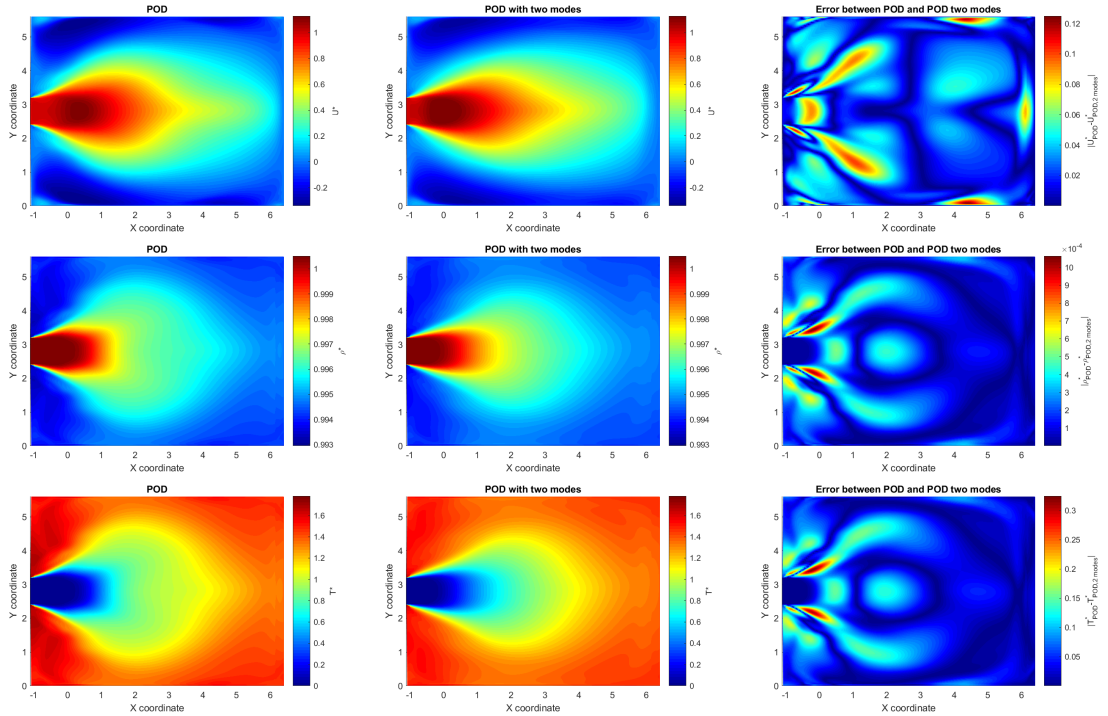

Figure 41: Velocity, density and temperature distributions on horizontal plane at 0.1 m above floor for $Ar = 7$.

From figure 41 it can be seen that most of the structures are reconstructed with only two modes, such as the acceleration region for the velocity u-component, decrease in temperature further into the room, and the non-dimensional density with relatively low error. Its expected higher error estimate for wall regions and main interaction zone since not all the energy is taken into the reconstruction using the POD based prediction method.

We can see that the error between POD and POD with two modes is sufficient low for all cases, (figure 42, 43 and 44). Some reduced accuracy is expected, since not all energy conserved by POD interpolation method is included, but all the essential flow features are captured as before.

6.4.2 POD-interpolation prediction for first two modes for $Ar = 15$

The results presented here show the similar trend as stated in last section. It shows sufficient lower error between POD and POD with two modes. POD with two modes capture most of the most dominant structures as expected. It is to be noted that we have used the cubic spline interpolation of the POD coefficients to construct/predict the flow variables for $Ar = 7$ and $Ar = 15$, other interpolation methods can be tested for error analysis.

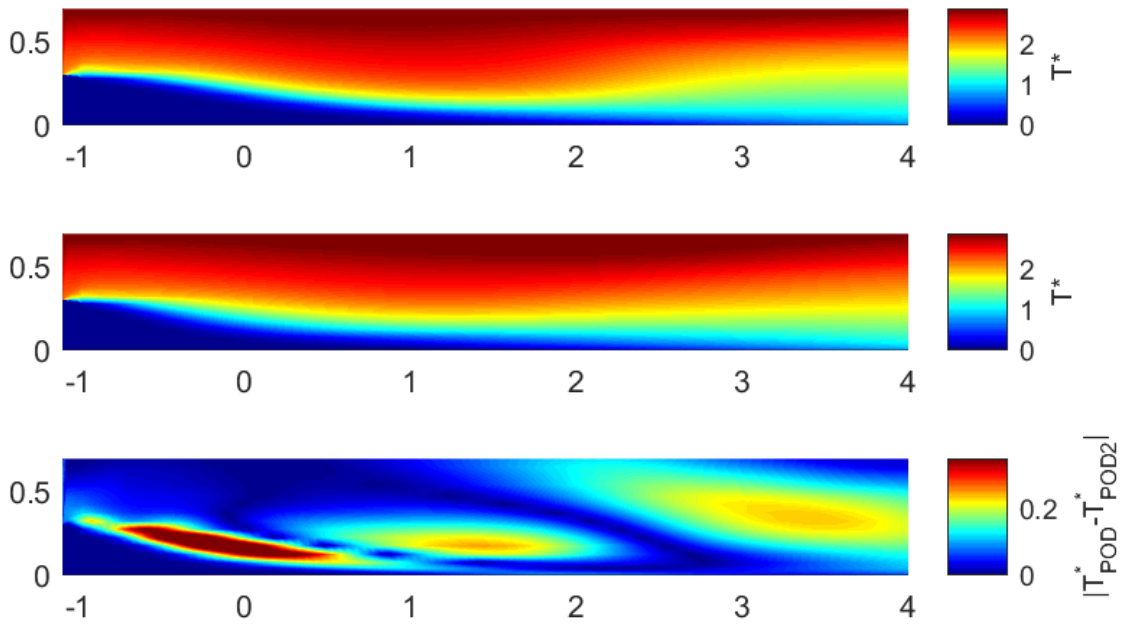

Figure 42: POD, POD with two modes and error estimates between POD and POD with two modes on a vertical plane for T^* at $y = 2.8$ for $Ar = 7$. Top: POD, middle: POD with two modes, bottom: Error estimate.

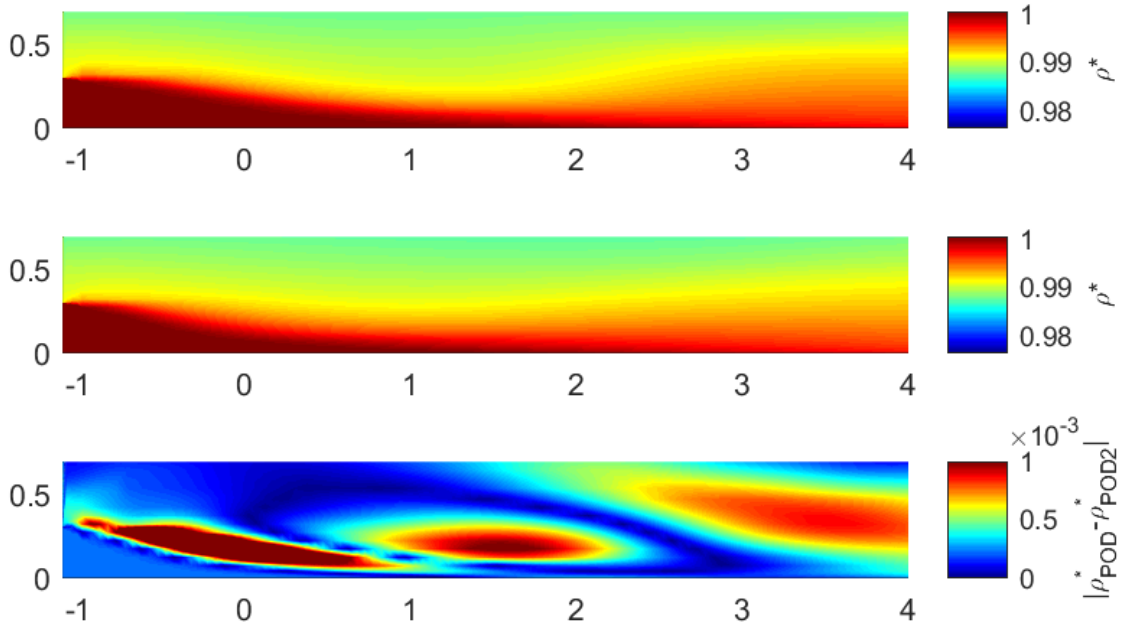

Figure 43: POD, POD with two modes and error estimates between POD and POD with two modes on a vertical plane for ρ^* at $y = 2.8$ for $Ar = 7$. Top: POD, middle: POD with two modes, bottom: Error estimate.

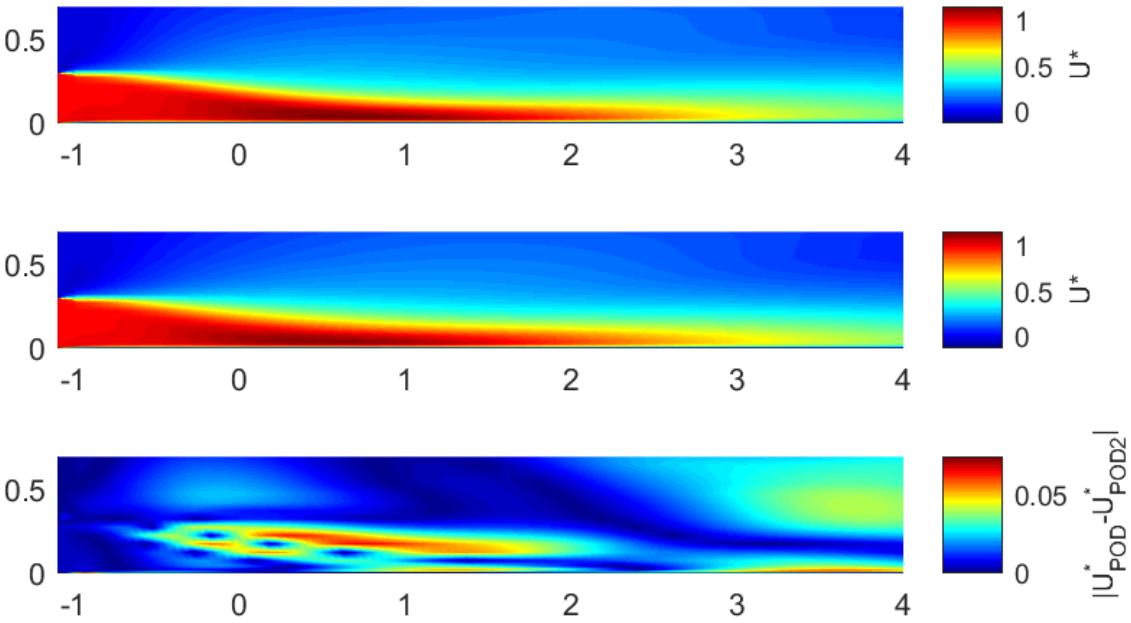

Figure 44: POD, POD with two modes and error estimates between POD and POD with two modes on a vertical plane for U^* at $y = 2.8$ for $Ar = 7$. Top: POD, middle: POD with two modes, bottom: Error estimate.

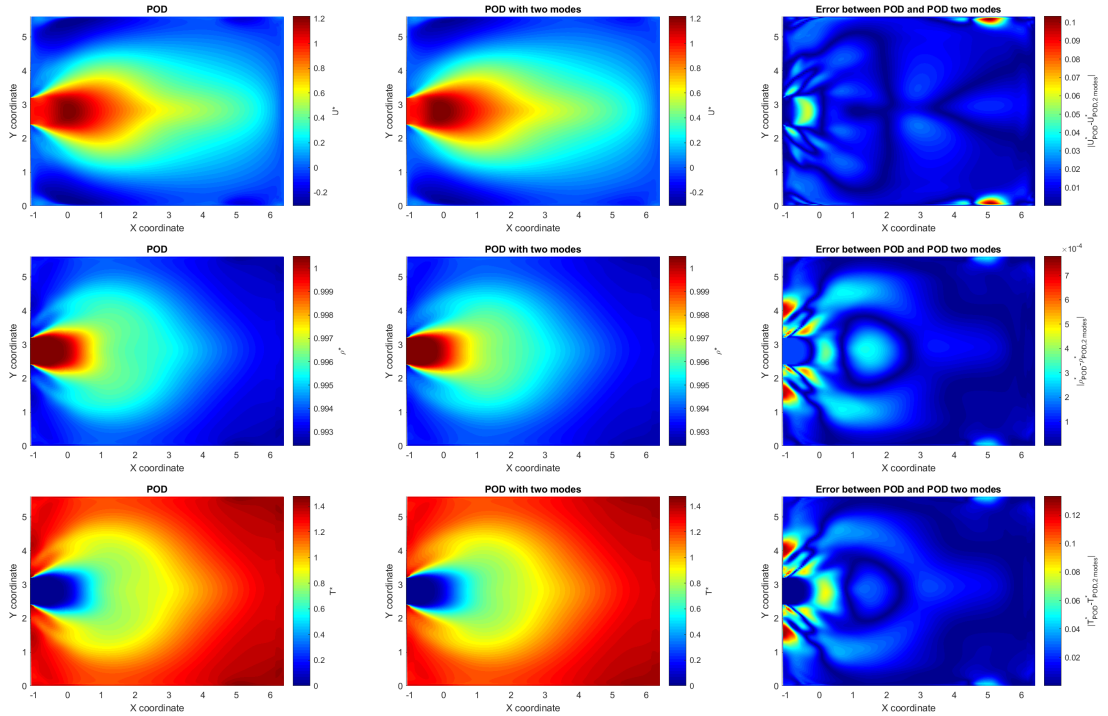

Figure 45: Velocity, density and temperature distributions on horizontal plane at 0.1 m above floor for $Ar = 15$.

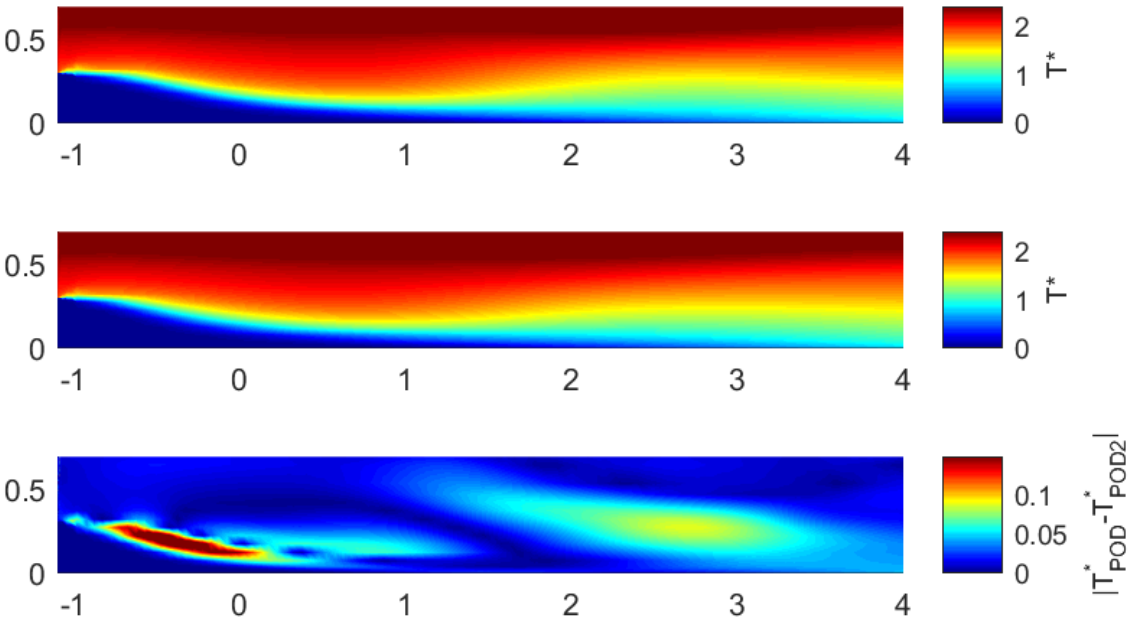

Figure 46: POD, POD with two modes and error estimates between POD and POD with two modes on a vertical plane for T^* at $y = 2.8$ for $Ar = 15$. Top: POD, middle: POD with two modes, bottom: Error estimate.

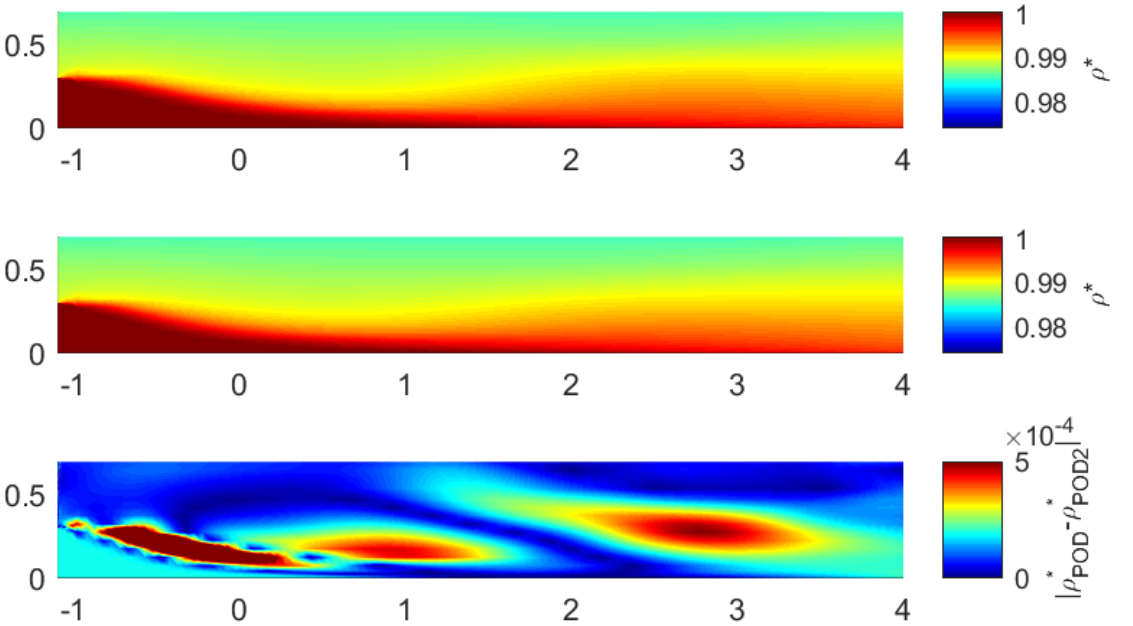

Figure 47: POD, POD with two modes and error estimates between POD and POD with two modes on a vertical plane for ρ^* at $y = 2.8$ for $Ar = 15$. Top: POD, middle: POD with two modes, bottom: Error estimate.

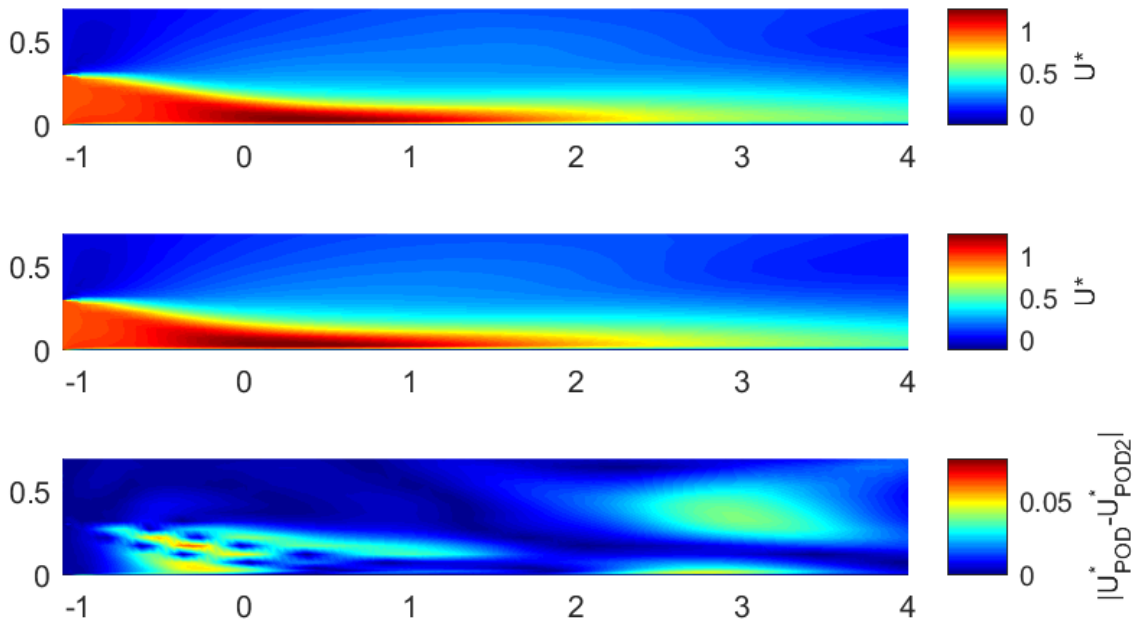

Figure 48: POD, POD with two modes and error estimates between POD and POD with two modes on a vertical plane for U^* at $y = 2.8$ for $Ar = 15$. Top: POD, middle: POD with two modes, bottom: Error estimate.

7 Conclusion

In this work, we have presented a POD-interpolation based methodology in resolving complex indoor airflow patterns and thermal stratification related to a DV system. A 2D thermal convection benchmark problem on a cavity geometry has been solved to verify and validate the overall implementation, which showed good results. The guideline of the Nordtest method is adopted to build the case studies associate with a DV-system configuration for a standard room. Steady-state CFD snapshots with varying Archimedes number are used to estimate the dominant POD coefficients/modal amplitudes and POD modes.The flow field variables are decomposed in terms of Archimedes number dependent POD coefficient and associated space dependent POD bases. A cubic spline interpolation of the POD coefficients is used to predict the solution for intermediate value of Archimedes number.

The CFD-study shows that we capture the most well known characteristics for a DV-system, such as acceleration zone and thermal stratification. Further on the POD interpolation analysis reveals that there is good agreement between visualization of ρ^*, T^* and U^* for CFD and POD. The analysis also revelas that for the u-componenet of the velocity field, the first two POD modes are the most dominant modes accounting the associated energy $\approx 99.5\%$, which means that one can estimate solutions for intermediate Archimedes numbers with good accuracy only using two modes.

The present study clearly shows the capability of CFD snapshot based POD-interpolated fast and reliable predictions of DV configuration involving a wall mounted linear air terminal device. A future study with the different types of air terminal devices and obstacles such as humans placed in the room could be undertaken and this fast prediction approach is potentially advantageous to carry out further parametric variations without performing large number of physical experiments and validate existing semi-empirical models of DV systems.

References

[1] Saiied M Aminossadati and Behzad Ghasemi. A numerical study of mixed convection in a horizontal channel with a discrete heat source in an open cavity. *European Journal of Mechanics-B/Fluids*, 28(4):590–598, 2009.

[2] Taha Arghand, Taghi Karimipanah, Hazim B Awbi, Mathias Cehlin, Ulf Larsson, and Elisabet Linden. An experimental investigation of the flow and comfort parameters for under-floor, confluent jets and mixing ventilation systems in an open-plan office. *Building and Environment*, 92:48–60, 2015.

[3] Steven L Brunton, Bernd R Noack, and Petros Koumoutsakos. Machine learning for fluid mechanics. *Annual Review of Fluid Mechanics*, 52:477–508, 2020.

[4] Guangyu Cao, Hazim Awbi, Runming Yao, Yunqing Fan, Kai Sirén, Risto Kosonen, and Jianshun Jensen Zhang. A review of the performance of different ventilation and airflow distribution systems in buildings. *Building and environment*, 73:171–186, 2014.

[5] Francesco Causone, Fabio Baldin, Bjarne W Olesen, and Stefano P Corgnati. Floor heating and cooling combined with displacement ventilation: Possibilities and limitations. *Energy and Buildings*, 42(12):2338–2352, 2010.

[6] Mathias Cehlin. *Visualization of air flow, temperature and concentration indoors: whole-field measuring methods and CFD*. PhD thesis, KTH, 2006.

[7] Mathias Cehlin and Bahram Moshfegh. Numerical modeling of a complex diffuser in a room with displacement ventilation. *Building and Environment*, 45(10):2240–2252, 2010.

[8] Narae Choi, Toshio Yamanaka, Kazunobu Sagara, Yoshihisa Momoi, and Tomoya Suzuki. Displacement ventilation with radiant panel for hospital wards: Measurement and prediction of the temperature and contaminant concentration profiles. *Building and Environment*, 160: 106197, 2019.

[9] Lars Davidson. Ventilation by displacement in a three-dimensional room—a numerical study. *Building and environment*, 24(4):363–372, 1989.

[10] Basman Elhadidi and H Ezzat Khalifa. Application of proper orthogonal decomposition to indoor airflows. *Ashrae Transactions*, 111(1), 2005.

[11] Sara Gilani, Hamid Montazeri, and Bert Blocken. Cfd simulation of stratified indoor environment in displacement ventilation: Validation and sensitivity analysis. *Building and Environment*, 95:299–313, 2016.

[12] Khalesi Javad and Goudarzi Navid. Thermal comfort investigation of stratified indoor environment in displacement ventilation: Climate-adaptive building with smart windows. *Sustainable Cities and Society*, 46:101354, 2019.

[13] H Ezzat Khalifa, Basman Elhadidi, and John F Dannenhoffer III. Efficient coupling of multizone and cfd indoor flow models through proper orthogonal decomposition. *ASHRAE Transactions*, 113(2), 2007.

[14] Yuguo Li, Mats Sandberg, and Laszlo Fuchs. Vertical temperature profiles in rooms ventilated

by displacement: Full-scale measurement and nodal modelling. *Indoor Air*, 2(4):225–243, 1992.

[15] Laurent Magnier, Radu Zmeureanu, and Dominique Derome. Experimental assessment of the velocity and temperature distribution in an indoor displacement ventilation jet. *Building and Environment*, 47:150–160, 2012.

[16] S. McKinley and M. Levine. Cubic spline interpolation. URL `https://www.rajgunesh.com/resources/downloads/numerical/cubicsplineinterpol.pdf`.

[17] María Alejandra Menchaca Brandan. *Study of airflow and thermal stratification in naturally ventilated rooms*. PhD thesis, Massachusetts Institute of Technology, 2012.

[18] Knud Erik Meyer, Jakob M Pedersen, and Oktay Özcan. A turbulent jet in crossflow analysed with proper orthogonal decomposition. *Journal of Fluid Mechanics*, 583:199–227, 2007.

[19] M.Gosling. Best practice design for displacement ventilation, 2017. URL `https://modbs.co.uk/news/fullstory.php/aid/17208/Best_practice_design_for__displacement_ventilation.html`.

[20] Peter V Nielsen. Displacement ventilation in a room with low-level diffusers. 1988.

[21] Peter V Nielsen. Velocity distribution in a room ventilated by displacement ventilation and wall-mounted air terminal devices. *Energy and Buildings*, 31(3):179–187, 2000.

[22] Nordtest. Air terminal devices: Aerodynamic testing and rating at low velocity (nt vvs 083), 2003.

[23] J. Solhaug P. Schild and M. Sandberg. Universal equations for testing and documenting aerodynamic performance of displacement ventilation units, 2003.

[24] Donghyun Rim. Transient simulation of airflow and pollutant dispersion under mixing flow and buoyancy driven flow regimes in residential buildings. *Ashrae Transactions*, 114:130, 2008.

[25] Fatih Selimefendigil. Numerical analysis and pod based interpolation of mixed convection heat transfer in horizontal channel with cavity heated from below. *Engineering Applications of Computational Fluid Mechanics*, 7(2):261–271, 2013.

[26] L Sirovich. Turbulence and the dynamics of coherent structures, parts i-iii. quart. of. *Appl. Math*, pages 561–582, 1987.

[27] Lawrence Sirovich and Michael Kirby. Low-dimensional procedure for the characterization of human faces. *Josa a*, 4(3):519–524, 1987.

[28] Henk Kaarle Versteeg and Weeratunge Malalasekera. *An introduction to computational fluid dynamics: the finite volume method*. Pearson education, 2007.

[29] Zhu Wang, Brian McBee, and Traian Iliescu. Approximate partitioned method of snapshots for pod. *Journal of Computational and Applied Mathematics*, 307:374–384, 2016.

[30] Guanqiong Wei, Bingqian Chen, Dayi Lai, and Qingyan Chen. An improved displacement ventilation system for a machining plant. *Atmospheric Environment*, page 117419, 2020.

[31] Xiaoxiong Yuan, Qingyan Chen, and Leon R Glicksman. A critical review of displacement ventilation. *ASHRAE Transactions-American Society of Heating Refrigerating Airconditioning Engin*, 104(1):78–90, 1998.